

Efficient detection of chaos through the computation of the Generalized Alignment Index (GALI) by the multi-particle method

Bertin Many Manda^{a,b}, Malcolm Hillebrand^{a,c,d}, Charalampos Skokos^a

^aNonlinear Dynamics and Chaos Group, Department of Mathematics and Applied Mathematics, University of Cape Town, Rondebosch, 7701 Cape Town, South Africa

^bLaboratoire d'Acoustique de l'Université du Mans (LAUM), UMR 6613, Institut d'Acoustique - Graduate School (IA-GS), CNRS, Le Mans Université, France

^cMax Planck Institute for the Physics of Complex Systems, Nöthnitzer Straße 38, 01187 Dresden, Germany

^dCenter for Systems Biology Dresden, Pfotenhauer Straße 108, 01307 Dresden, Germany

Abstract

We present a thorough analysis of computing the Generalized Alignment Index (GALI), a rapid and effective chaos indicator, through a simple multi-particle approach, which avoids the use of variational equations. We develop a theoretical leading-order estimation of the error in the computed GALI for both the variational method (VM) and the multi-particle method (MPM), and confirm its predictions through extensive numerical simulations of two well-known Hamiltonian models: the Hénon-Heiles and the β -Fermi-Pasta-Ulam-Tsingou systems. For these models the GALIs of several orders are computed and the MPM results are compared to the VM outcomes. The dependence of the accuracy of the MPM on the renormalization time, integration time step, as well as the deviation vector size, is studied in detail. We find that the implementation of the MPM in double machine precision ($\varepsilon \approx 10^{-16}$) is reliable for deviation vector magnitudes centred around $d_0 \approx \varepsilon^{1/2}$, renormalization times $\tau \lesssim 1$, and relative energy errors $E_r \lesssim \varepsilon^{1/2}$. These results are valid for systems with many degrees of freedom and for several orders of the GALIs, with the MPM particularly capturing very accurately the GALI_2 behavior. Our results show that the computation of the GALIs by the MPM is a robust and efficient method for investigating the global chaotic dynamics of autonomous Hamiltonian systems, something which is of distinct importance in cases where it is difficult to explicitly write the system's variational equation or when these equations are too cumbersome.

1. Introduction

Revealing the properties of individual or ensembles of orbits belonging to particular phase space region is of fundamental interest for nonlinear systems. One of the most prominent tools for this task are *chaos indicators*, which are real-valued quantities exhibiting distinct behaviors for different dynamical evolutions [1, 2, 3, 4].

Over the last fifty years, several chaos detection techniques have been developed and employed in a wide variety of fields. The Lyapunov exponents (LEs) [5, 6] for example, have become a well-established cornerstone in understanding and quantifying chaos in nonlinear systems (see e.g. [7, 3, 8] and references therein). Alongside with them, other chaos detection techniques, such as the fast Lyapunov indicator (FLI) [9, 10], the mean exponential growth of nearby orbits (MEGNO) [11, 12] the smaller (SALI) and generalized (GALI) alignment indices [13, 14, 15], to name a few, have found applications in information theory [16], biophysics and materials [17, 18, 19], astrophysics [20, 21, 22], as well as population dynamics and epidemiology [23, 24]. In these works, the utility of each indicator in a different context was shown, emphasizing the efficiency with which the accurate chaos detection was achieved [14, 22]. This wide-ranging applicability of chaos indicators provides strong motivation for probing their evaluation, whether through optimising the numerical pro-

cedures [25, 26, 27], choosing appropriate methods of calculation [28, 29], or using short time computations to determine chaoticity [30]. Being able to reliably and efficiently evaluate these indicators in a variety of systems is of significant importance.

The majority of these chaos indicators rely on the time evolution of initially neighboring orbits to the trajectory under study. Depending on whether the neighboring orbits are kept in the vicinity or are driven away from the system's reference orbit allows the characterization of the studied orbit's long-time stability. In order to numerically evolve these initially nearby orbits, two methods are usually implemented. In the first case, alongside the system's reference orbit, several initially nearby trajectories are evolved by numerically solving the system's equations of motion. This is done in such a way that the time evolution of the separation vectors between the studied orbit and its neighbors can be tracked for all time, so that these vectors can be used to estimate the spatiotemporal properties of chaos indicators. A second approach is based on the fact that the initial separation vectors are by definition considered to be very small. Consequently their dynamics can be approximated by a linearization of the system's equations of motion along the studied orbit. The equations obtained by this approximation are referred to as *variational equations*. In this work we name the former approach the multi-particle method (MPM) and the latter the variational method (VM).

Nowadays the VM is the most commonly used method, mainly due to its accuracy and simplicity. This approach relies on the explicit derivation of the variational equations, which requires the dynamical system's force field to be continuous and differentiable over the considered space-time domain, something which is not always the case. As an example we can mention a model whose particles' interactions are described via Hertzian contacts [31], or simply consider discontinuous or non-analytic force fields related to work softening [32, 33] and hardening [34, 35] laws. Furthermore, the ever increasing complexity of the equations describing the system's dynamics in modern physical models makes the derivations of the variational equations difficult (see e.g. [19]). Thus, occasionally, even in cases where the variational equations can be explicitly expressed in closed analytical forms, their complexity could result to strains during the code implementation due to difficulties with respect to the code optimization (because of its large size), and due to the increase of computational times, as complex variational equations can considerably increase the number of basic computer operations.

The MPM can be implemented in a variety of cases, and seems to be particularly advantageous whenever the VM's use becomes problematic, since it requires only the knowledge of the system's equations of motion. Nevertheless, the results obtained from the MPM must always be treated with care because they are known to lead to spurious estimates, see Ref. [28] for examples in astrophysics. Consequently several studies of the reliability of the MPM for the computation of the MLE have already been carried out [28, 26, 29] (see also Sect. 3.5 of [3]). On the other hand, some more recently introduced chaos indicators such as the GALI method, have only been used in the framework of the VM. It follows that its definitions, reliability and computational performances in the context of the MPM has, to the best of our knowledge, never been examined.

The aim of our study is to investigate the reliability of the GALI computation through the MPM. We start our analysis by demonstrating that the definitions of the GALI using the VM (see e.g. [14]) and the MPM are equivalent. Then, we obtain leading order analytical expressions of the numerical accuracy during the computation of the GALI values for both methods. We find that our analytical results are validated by simulating the short-time dynamics of some well-known, prototypical nonlinear Hamiltonian systems: the Hénon-Heiles (HH) [36] and β -Fermi-Pasta-Ulam-Tsingou (β -FPUT) [37, 38] systems. Moreover, using the parameter values which we found to optimize the performance of the MPM, we show that the GALI method is in general able to characterize with good accuracy the nature of the orbits of the studied systems.

We also examine the ability of the GALI method to reveal the global dynamics of Hamiltonian systems. We find that the mapping of a slice of the phase space of the HH system obtained using the Poincaré surface of section (PSS) technique [39] and the GALI method leads to the same qualitative features in the identification of regions of regular and chaotic motion. In addition, by recording the central processing unit (CPU) time needed to perform the scan of the PSS using the GALI and the MLE implemented with the MPM, we show that the GALI method is

still faster compared to the MLE in performing this task.

The content of the paper is organized as follows. Section 2 contains a brief introduction to the LE and GALI. In Sect. 3, we present the theoretical analysis for the accumulation of numerical errors in the computation of the GALI. In Sec. 4, we examine the conditions of reliability for the computation of the GALI using both the VM and MPM, focusing on regular and chaotic orbits of the HH and the β -FPUT models. Finally in Sec. 5, we summarize our findings and discuss some open questions. In the appendices, we provide a number of details relevant to this work, including the pseudo code for the computation of GALI using the MPM, initial conditions and additional GALI results for the FPUT model.

2. Lyapunov exponents (LEs) and the Generalized Alignment index (GALI)

In our study we consider autonomous Hamiltonian systems of N degrees of freedom, which are defined by a Hamiltonian function (whose numerical value is typically called the system's energy) of the form

$$\mathcal{H}(q_1, q_2, \dots, q_N, p_1, p_2, \dots, p_N) = \mathcal{H}(\mathbf{x}), \quad (1)$$

where q_i and p_i , $i = 1, 2, \dots, N$ respectively are the generalized canonical coordinates and momenta of the system and $\mathbf{x} = (x_1, x_2, \dots, x_N, x_{N+1}, \dots, x_{2N}) = (q_1, q_2, \dots, q_N, p_1, \dots, p_N)$ is a state vector in the system's phase space. The equations of motion are given by

$$\dot{\mathbf{x}} = \mathbf{J}_{2N} \cdot \frac{\partial \mathcal{H}}{\partial \mathbf{x}} = \mathbf{f}(\mathbf{x}), \quad (2)$$

with

$$\mathbf{J}_{2N} = \begin{pmatrix} \mathbf{0}_N & \mathbf{I}_N \\ -\mathbf{I}_N & \mathbf{0}_N \end{pmatrix}, \quad (3)$$

being the so-called symplectic matrix, where $\mathbf{0}_N$ and \mathbf{I}_N are the $N \times N$ null and identity matrices respectively. In Eq. (2), the over-dot denotes the derivative with respect to time t . Considering an initial condition \mathbf{x}_0 at time t_0 , the solution of Eq. (2), $\mathbf{x}(t)$, $t > 0$, conserves the value of the system's energy \mathcal{H} Eq. (1). In addition, we set $t_0 = 0$.

Let us k orthogonal small deviation vectors from a system's reference orbit \mathbf{x} , namely $\delta\mathbf{x}_1, \delta\mathbf{x}_2, \dots, \delta\mathbf{x}_k$, we define the k th finite-time LEs

$$\lambda_k(t) = \frac{1}{t} \ln \frac{\|\delta\mathbf{x}_k(t)\|}{\|\delta\mathbf{x}_k(0)\|}, \quad (4)$$

which quantifies the exponential rate of growth of the k th deviation vector. Here $t = R\tau$, where R is a positive integer and τ the renormalization time, i.e., the time interval after which the LE is computed. Further, the $\|\cdot\|$ stands for the usual Euclidean norm and $\delta\mathbf{x}_k = (\delta x_{k,1}, \delta x_{k,2}, \dots, \delta x_{k,N}, \delta x_{k,N+1}, \dots, \delta x_{k,2N-1}, \delta x_{k,2N})$. As such the

$$\Lambda_k = \lim_{t \rightarrow \infty} \lim_{\delta\mathbf{x}_k(0) \rightarrow 0} \lambda_k(t), \quad (5)$$

are called Lyapunov exponents. As Λ_k is unreachable for practical computation, we mainly rely on the $\lambda_k(t)$ at $t \gg 1$ for their approximation. Thus, we use the fact that the finite-time LEs

$\lambda_k(t) \propto t^{-1} \ln t$ for regular trajectories, and approaches a constant for chaotic trajectories.

Instead of monitoring the rate of growth of each deviation vector, we can also look at the alignments between all of them. Then the GALI of order k (GALI_k) measures the volume of the generalized parallelepiped whose edges are the corresponding k unit vectors $\widehat{\delta \mathbf{x}}_k(t) = \delta \mathbf{x}_k(t) / \|\delta \mathbf{x}_k(t)\|$, and is given by

$$\text{GALI}_k(t) = \|\widehat{\delta \mathbf{x}}_1(t) \wedge \widehat{\delta \mathbf{x}}_2(t) \wedge \dots \wedge \widehat{\delta \mathbf{x}}_k(t)\|, \quad (6)$$

where ‘ \wedge ’ denotes the wedge product of vectors and $t = R\tau$.

The ability of the GALI to distinguish between regular and chaotic orbits was theoretically explained in [14] and has been demonstrated in several applications of the index to various dynamical systems [40, 41, 42]. More specifically, the time evolution of GALI_k for a regular orbit is [14, 43, 15]

$$\text{GALI}_k(t) \propto \begin{cases} \text{constant} & \text{if } 2 \leq k \leq N \\ t^{-2(k-N)} & \text{if } N < k \leq 2N \end{cases}, \quad (7)$$

i.e., the index either remains practically constant for $2 \leq k \leq N$, or decays to zero following a power law evolution for $N < k \leq 2N$. On the other hand, for chaotic orbits GALI_k decrease exponentially fast to zero with an exponent which depends on the values of the k largest LEs $\lambda_1 \geq \lambda_2 \geq \dots \geq \lambda_k$ [14]

$$\text{GALI}_k(t) \propto \exp\left(-t \sum_{i=2}^k (\lambda_1 - \lambda_i)\right). \quad (8)$$

3. Theoretical estimations of the GALI’s numerical evaluation

Our aim is to investigate the numerical errors arising during the numerical computation of the GALI using the MPM and VM. Before proceeding we outline a number of assumptions aiming to simplify our analysis. In the rest of this section we assume the volume formed by the unit tangent vectors to the reference orbits, i.e. the GALI value at any time of the system’s evolution is bounded by the one of a right angled parallelepiped with side the same unit tangent vectors. It follows that it is enough to focus on the product of the magnitudes of the tangent vectors as it shares the same numerical error with GALI up to a multiplicative factor which depends on the orientations between the different tangent vectors.

Furthermore, given that all the tangent vectors to the reference orbit have initially the same magnitude, and due to the fact that they are evolved independently, we will consider that the numerical error accumulates equally for all the tangent vectors. That is to say, it is sufficient to evaluate the numerical errors of one single vector to deduce the numerical errors during the computation of the volume formed by all the tangent vectors, which is proportional to (or of the same order as) GALI.

In addition, we roughly consider that the origin of the numerical errors stems from three main contributions which are independent for all times: (i) the machine precision, (ii) the magnitude of the tangent vectors at the renormalization time

(iii) and the global truncation errors of the numerical integration schemes [29]. It follows that the numerical uncertainty for the GALI_k is complex and expressed as a multivariate polynomial of order k whose variables are all factors influencing the numerical evolution of the phase space and tangent vectors. In order to analyse the error meaningfully, we consequently focus only on the leading order terms, because they are simple and depend on the main *extensive parameters* influencing the evolution of the tangent vectors. We will show that such terms are the primary contributors to the numerical inaccuracies of the computed GALI in short-time scales.

For completeness, we point toward additional notes relevant to this work in the literature. The effects of the global truncation errors of the numerical integration scheme, the length of the initial tangent vectors, the renormalization time and the machine precision on the computation of the MLE are investigated in Ref. [29]. Furthermore, in Sec. 3.5 of Ref. [3] (and references therein), additional sources of numerical errors in the computation of the LEs are studied. For instance, the numerical orthogonalization’s related errors and the statistical errors due to the finite time computations of the LEs. In the case of the GALI method, the effects of the numerical integration techniques during its numerical computation are briefly investigated by Ref. [26].

3.0.1. The variational method

In this section, we focus on evaluating the numerical uncertainty of the computation of GALI using the variational approach. It is worth noting that the VM constitutes the sole approach considered in previous studies (see e.g. [14, 15]) for the computation of the GALI. Thus later, we will prove that the definition of the GALI in the variational framework is equivalent to the definition using the MPM. The variational equations are obtained by linearizing the equations of motion [Eq. (2)] around a reference orbit $\mathbf{x}(t)$ in the phase space. Considering a set of k orthogonal deviation (tangent) vectors

$$\begin{aligned} \mathbf{w}_i(t_0) &= \delta \mathbf{x}_i(t_0) = \left(\delta x_{i,1}(t_0), \delta x_{i,2}(t_0), \dots, \delta x_{i,N}(t_0), \right. \\ &\quad \left. \delta x_{i,N+1}(t_0), \dots, \delta x_{i,2N-1}(t_0), \delta x_{i,2N}(t_0) \right) \\ &= \left(w_{i,1}(t_0), w_{i,2}(t_0), \dots, w_{i,N}(t_0), \right. \\ &\quad \left. w_{i,N+1}(t_0), w_{i,N+2}(t_0), \dots, w_{i,2N}(t_0) \right) \end{aligned}$$

to the system’s orbit \mathbf{x}_0 in phase space, the variational equations are made up of $2kN$ differential forms

$$\dot{\mathbf{w}}_i = \mathbf{J}_{2N} \cdot \mathbf{D}^2 \mathcal{H}(\mathbf{x}(t)) \cdot \mathbf{w}_i = \frac{\partial \mathbf{f}(\mathbf{x}(t))}{\partial \mathbf{x}} \cdot \mathbf{w}_i = \mathbf{A}(t) \cdot \mathbf{w}_i, \quad (9)$$

where $\mathbf{D}^2 \mathcal{H}(\mathbf{x}(t))$ is the Hessian matrix of the Hamiltonian evaluated at the reference orbit $\mathbf{x}(t)$, and the subscript i indexes the tangent vector. As initial conditions for the variational equations, the common practice is to choose random coordinates for the deviation vectors, which are then rescaled in such a way that they all share the same norm, i.e. $\|\mathbf{w}_i(0)\| = \|\mathbf{w}_{i,0}\| = d_0$ ($d_0 > 0$).

The formal solution of Eq. (9) reads

$$\mathbf{w}_i(t) = \exp\left[\int_0^t \mathbf{A}(t')dt'\right] \cdot \mathbf{w}_i(0). \quad (10)$$

In what follows, we first assume that the trajectory of the system $\mathbf{x}(t)$ and its tangent dynamics $\mathbf{w}_i(t)$ are known in a closed form. Consequently, we define the GALI of order k (denoted as G_k for the VM) of the orbit \mathbf{x} after a renormalization time τ [14, 15]

$$G_k(\tau) = \|\mathbf{u}_1(\tau) \wedge \mathbf{u}_2(\tau) \wedge \dots \wedge \mathbf{u}_k(\tau)\|, \quad (11)$$

where

$$\mathbf{u}_i(\tau) = \frac{\mathbf{w}_i(\tau)}{\|\mathbf{w}_i(\tau)\|}, \quad (12)$$

is the unit vector of the i^{th} deviation vector $\mathbf{w}_i(t)$.

We first investigate the error due to the machine precision (referred to as ε) during the computation of GALI after one renormalization time τ denoted as $G_k(\tau, \varepsilon)$. Starting from unit deviation vectors, i.e. $d_0 = 1$ and assuming that the renormalization time τ is small, we have $\|\mathbf{w}_i(\tau)\| \approx 1$ such that

$$\widetilde{u}_{i,m}(\tau) = u_{i,m}(\tau) + \mathcal{O}(\varepsilon), \quad (13)$$

with $\widetilde{u}_{i,m}$ denoting the machine representation of $u_{i,m}$. In general, we will denote by \widetilde{Q} any approximation of the variable Q . Thus the computer representation of the GALI of order k writes

$$\widetilde{G}_k(\tau, \varepsilon) = \|\widetilde{\mathbf{u}}_1(\tau) \wedge \widetilde{\mathbf{u}}_2(\tau) \wedge \dots \wedge \widetilde{\mathbf{u}}_k(\tau)\|, \quad (14)$$

in such a way that the error due to the machine precision writes

$$\widetilde{G}_k(\tau, \varepsilon) - G_k(\tau) = \mathcal{O}(\varepsilon^k). \quad (15)$$

In addition to effect of the machine precision on the computation of GALI, the magnitude of the initial deviation vectors $d_0 = \|\mathbf{w}_i(t_0)\|$ also impacts the computed GALI values at each renormalization time. By denoting $\widetilde{G}_k(\tau, \rho)$ the GALI obtained by replacing $\mathbf{w}_i(t_0)$ by $\mathbf{w}_i^\rho(t_0) = \rho \cdot \|\mathbf{w}_i(t_0)\|$ where $\rho = d_0 / \|\mathbf{w}_i(t_0)\|$ is the rescaling factor, we see that the time evolution of the rescaled deviation vectors $\mathbf{w}_i^\rho(t)$ is given by

$$\mathbf{w}_i^\rho(t) = \rho \mathbf{w}_i(t), \quad (16)$$

with the time evolution of $\mathbf{w}_i(t)$ being generated by the solution to the variational equations [Eq. (10)]. Consequently,

$$\mathbf{u}_i^\rho(\tau) = \frac{\mathbf{w}_i^\rho(\tau)}{\|\mathbf{w}_i^\rho(\tau)\|} = \frac{\rho \mathbf{w}_i(\tau)}{\|\rho \mathbf{w}_i(\tau)\|} = \frac{\mathbf{w}_i(\tau)}{\|\mathbf{w}_i(\tau)\|} = \mathbf{u}_i(\tau), \quad (17)$$

and the magnitude of the k initial deviation vectors do not affect the calculations of GALI in case of the VM. In this context, we only have to take into account round off errors for the computer representation of \mathbf{u}_i^ρ , similar to what was done in Eq. (13). Thus the numerical inaccuracy of the GALI at the renormalization time due to the magnitude of the deviation vectors leads to

$$\widetilde{G}_k(\tau, \rho) - G_k(\tau) = \mathcal{O}(\varepsilon^k). \quad (18)$$

Combining the errors due to machine precision [Eq. (15)] and the ones due to the magnitude of the deviation vectors at the renormalization time [Eq. (18)] leads to

$$\widetilde{G}_k(\tau) - G_k(\tau) = \mathcal{O}(\varepsilon^k). \quad (19)$$

3.1. Multi-particle method

We can also define the GALI $_k$ in the framework of the MPM. Starting from the initial condition $\mathbf{x}(t_0) = \mathbf{x}_0$ and the k initially orthogonal separation (tangent) vectors

$$\begin{aligned} \mathbf{d}_i(t_0) &= \delta \mathbf{x}_i = (\delta x_{i,1}(t_0), \delta x_{i,2}(t_0), \dots, \delta x_{i,N}(t_0), \\ &\quad \delta x_{i,N+1}(t_0), \dots, \delta x_{i,2N-1}(t_0), \delta x_{i,2N}(t_0)) \\ &= (d_{i,1}(t_0), d_{i,2}(t_0), \dots, d_{i,N}(t_0), \\ &\quad d_{i,N+1}(t_0), d_{i,N+2}(t_0), \dots, d_{i,2N}(t_0)) \end{aligned}$$

with norm $\|\mathbf{d}_i(t_0)\| = d_0$, the orbit $\mathbf{x}(t)$ and its neighboring orbits $\mathbf{y}_i(t) = \mathbf{x}(t) + \mathbf{d}_i(t)$ can be obtained by integrating the equations of motion [Eq. (2)] $k + 1$ times. In this context, the GALI of order k (referred to as J_k for the MPM) is defined as

$$J_k(\tau) = \|\mathbf{v}_1(\tau) \wedge \mathbf{v}_2(\tau) \wedge \dots \wedge \mathbf{v}_k(\tau)\|, \quad (20)$$

at every renormalization time τ , with

$$\mathbf{v}_i(\tau) = \frac{\mathbf{d}_i(\tau)}{\|\mathbf{d}_i(\tau)\|}, \quad (21)$$

the unit vector of the i^{th} separation vector in the phase space. Our first task here is to show that Eq. (20) is equivalent to Eq. (11) i.e. $J_k(\tau) = G_k(\tau)$, so that the GALI defined using the VM and the MPM are equal.

In order to achieve our goal, we must find ways to approximate the evolution of the $\mathbf{d}_i(0)$. We use a Taylor series expansion

$$\dot{\mathbf{d}}_i \approx \mathbf{A}(t)\mathbf{d}_i + \frac{D^2 \mathbf{f}(\mathbf{x})}{2} \mathbf{d}_i^2 + \mathcal{O}(\|\mathbf{d}_i\|^3), \quad (22)$$

to approximate the time evolution of \mathbf{d}_i with $\mathcal{O}(\|\mathbf{d}_i\|^3) \rightarrow 0$, because the $\|\mathbf{d}_i\| \ll 1$. At this point, it is convenient for us to approximate the evolution of each element $d_{i,m}$ of the separation vectors with index i by the dynamics of its fastest changing coordinate corresponding to the direction of maximal stretching of the tangent vectors with rate of growth being the MLE [7]. Thus Eq. (22) can be simplified to

$$\dot{d}_{i,m}(t) \approx \lambda_1 d_{i,m}(t) + \Gamma d_{i,m}^2(t), \quad (23)$$

with λ_1 being the MLE and Γ a scaling coefficient of the second order derivative in the Taylor expansion [Eq. (22)]. Without loss of generality, we fix $\Gamma = \mathcal{O}(1)$.

Equation (23) can be solved analytically, considering an initial perturbation $d_{i,m}(t_0) \propto d_0$ at time $t_0 = 0$. Its solution can be written as

$$d_{i,m}(t) \approx \frac{\lambda_1 d_0 e^{\lambda_1 t}}{\lambda_1 + d_0 (1 - e^{\lambda_1 t})}, \quad (24)$$

which can be simplified to

$$d_{i,m}(t) \approx d_0 e^{\lambda_1 t} + d_0^2 t e^{\lambda_1 t} + \frac{1}{2} d_0^3 \lambda_1^2 t^2 e^{\lambda_1 t} + \mathcal{O}(d_0^3 t^2 e^{\lambda_1 t}), \quad (25)$$

with $\mathcal{O}(d_0^3 t^2 e^{\lambda_1 t}) \rightarrow 0$ again because $d_0 \ll 1$. It follows that, the first term on the right hand side of Eq. (25) represents the asymptotic solution [Eq. (10)] of the variational equations

[Eq. (9)] in the limit of large time, as also pointed out for example in Eq. (30) of Ref. [14], i.e. $\mathbf{w}_i(t) \approx \mathbf{w}_0 e^{\lambda_1 t}$. As a result, we write

$$d_{i,m}(t) \approx w_{i,m}(t) + d_0^2 t e^{\lambda_1 t} + \frac{1}{2} d_0^2 \lambda_1 t^2 e^{\lambda_1 t}. \quad (26)$$

Now let us turn back to expressing J_k [Eq. (20)] after one renormalization time τ . In order to address that question, we note that for small enough values of τ , we have $\|\delta_i(\tau)\| \approx \|\mathbf{w}_i(\tau)\| \approx d_0$ leading to

$$v_{i,m}(\tau) \approx \frac{d_{i,m}(\tau)}{d_0}, \quad u_{i,m}(\tau) \approx \frac{w_{i,m}(\tau)}{d_0}. \quad (27)$$

Consequently, we write based on Eq. (26) and Eq. (27)

$$\mathbf{v}_i(\tau) - \mathbf{w}_i(\tau) \approx \frac{1}{d_0} \mathbf{\Omega}, \quad (28)$$

where $\mathbf{\Omega}$ is the vector with coordinates $\Omega_m \approx d_0^2 \tau e^{\lambda_1 \tau} + \frac{1}{2} d_0^2 \lambda_1 \tau^2 e^{\lambda_1 \tau}$. This results in

$$J_k(\tau) \approx G_k(\tau) + \mathcal{O}(d_0^k \tau^k) + \mathcal{O}(d_0^k \tau^{2k}), \quad (29)$$

where we consider only leading orders. Therefore, it turns out that for $d_0 \rightarrow 0$, the GALI as defined using the VM and the MPM practically coincide for fixed τ .

Let us now look at the different numerical inaccuracies in computing the GALI in case of the MPM [Eq. (20)]. We first investigate the influence of machine precision when computing GALI after one renormalization time τ , i.e.

$$\tilde{J}_k(\tau, \varepsilon) = \|\tilde{\mathbf{v}}_1(\tau) \wedge \tilde{\mathbf{v}}_2(\tau) \wedge \dots \wedge \tilde{\mathbf{v}}_k(\tau)\|. \quad (30)$$

Clearly, as for the VM [see Eq. (14)], we find

$$\tilde{J}_k(\tau, \varepsilon) - J_k(\tau) = \mathcal{O}(\varepsilon^k). \quad (31)$$

The magnitude of the initial separation vectors at the renormalization time [Eq. (21)] also impacts the computation of the GALI using the MPM. If we assume that the reference orbit $\mathbf{x}(t)$ is bounded (i.e. an orbit which does not blow up to infinity) then $\tilde{\mathbf{x}}_m(t) = \mathbf{x}_m(t) + \mathcal{O}(\varepsilon)$ for all time, which also applies for all neighboring orbits $\mathbf{y}_i(t)$. As a result,

$$\tilde{d}_{i,m}(t) = \tilde{y}_{i,m}(t) - \tilde{x}_m(t) = d_{i,m}(t) + \mathcal{O}(\varepsilon). \quad (32)$$

with $y_{i,m}$ being phase space coordinates of the i^{th} nearby orbits from the reference orbit with element x_m . Consequently, the renormalization procedure [Eq. (21)] gives

$$\tilde{\mathbf{v}}_i(\tau) = \frac{\tilde{d}_i(\tau)}{\|\tilde{d}_i(\tau)\|} \approx \frac{d_i(\tau) + \mathcal{O}(\varepsilon)}{d_0} = \mathbf{v}_i(\tau) + \mathcal{O}\left(\frac{\varepsilon}{d_0}\right), \quad (33)$$

so that the leading order term in the numerical error of the GALI due to the magnitude of the separation vector reads

$$\tilde{J}_k(\tau, \rho) - J_k(\tau) = \mathcal{O}\left(\frac{\varepsilon^k}{d_0^k}\right). \quad (34)$$

Gathering together Eq. (29), Eq. (30) and Eq. (34) leads to

$$\tilde{J}_k(\tau) - G_k(\tau) = \mathcal{O}(d_0^k \tau^k) + \mathcal{O}(d_0^k \tau^{2k}) + \mathcal{O}\left(\frac{\varepsilon^k}{d_0^k}\right) + \mathcal{O}(\varepsilon^k). \quad (35)$$

3.2. Dependence of the GALI on the global numerical truncation errors

In the previous calculations, we worked assuming that we know the analytical form of the solution of the phase space and its associated tangent dynamics [Eq. (2)]. Nevertheless, for most models in nonlinear dynamics, the exact solution cannot be obtained. Therefore, we approximate the analytical solution of the system by a numerical one so that truncation errors introduced by the numerical integration scheme during the evolution of the orbit and its tangent space can be accounted for in the computation of the GALI.

In Ref. [29], it was argued that a numerical scheme of order p , with fixed integration time step h , affects the time propagation of the tangent vectors at time T by a term $\varepsilon_T = \mathcal{O}(h^p)$. This term accounts for the global truncation error on each tangent vector at time T . Then, the numerical error of the GALI when including the global truncation errors can be obtained following the same steps as above, leading to

$$\tilde{G}_k - \text{GALI}_k = \mathcal{O}(\varepsilon^k) + \mathcal{O}(\varepsilon_T^k), \quad (36)$$

when computing GALI using the VM. On the other hand, when the MPM is used, we have

$$\tilde{J}_k - \text{GALI}_k = \mathcal{O}(d_0^k \tau^k) + \mathcal{O}(d_0^k \tau^{2k}) + \mathcal{O}\left(\frac{\varepsilon^k}{d_0^k}\right) + \mathcal{O}(\varepsilon^k) + \mathcal{O}(\varepsilon_T^k). \quad (37)$$

In Fig. 1, we plot the dependence of the GALI_k against d_0 at fixed $\tau = 1$ value. The diagrams obtained define the reliable regions of GALI_k , by estimating the expressions of Eq. (36), the blue filled-triangles and Eq. (37), the red filled-circles. More specifically, we examine two cases namely when $\varepsilon < \varepsilon_T < \varepsilon^{1/2}$ shown in Fig. 1(a), and $\varepsilon_T > \varepsilon^{1/2}$ in Fig. 1(b). Note that in Fig. 1, the $\nu = \log_{10} \varepsilon$ and $\sigma = \log_{10} \varepsilon_T$. Overall, we see that reliable regions for the computation of GALI are independent of the GALI order. In addition the GALI_k computed using the VM is independent of the magnitude of the initial tangent vectors d_0 , Figs. 1(a-b). In fact, in this case the computed values of the GALI only depend on the global truncation error ε_T of the numerical integration scheme, since the latter is general much larger than the machine precision ε .

On the other hand, the results of the reliable regions using the MPM can be separated in two cases. Whether $\varepsilon_T \in [\varepsilon, \varepsilon^{1/2}]$, we obtain a V-shape with minimum located at $d_0 \sim \varepsilon^{1/2}$, red curve in Fig. 1(a). In addition, when $\varepsilon_T > \varepsilon$, the V-shape loses its pointy edge for a flat bottom, which means that the most accurate results using the MPM is also dependent on the ε_T value, Fig. 1(b).

4. Numerical results

4.1. Hamiltonian models and computational setup

The first model of our interest is the well known two-dimensional (2D) HH system, whose Hamiltonian function reads [36, 44]

$$\mathcal{H} = \frac{1}{2} (p_1^2 + p_2^2) + \frac{1}{2} (x_1^2 + x_2^2) + x_1^2 x_2 - \frac{1}{3} x_2^3, \quad (38)$$

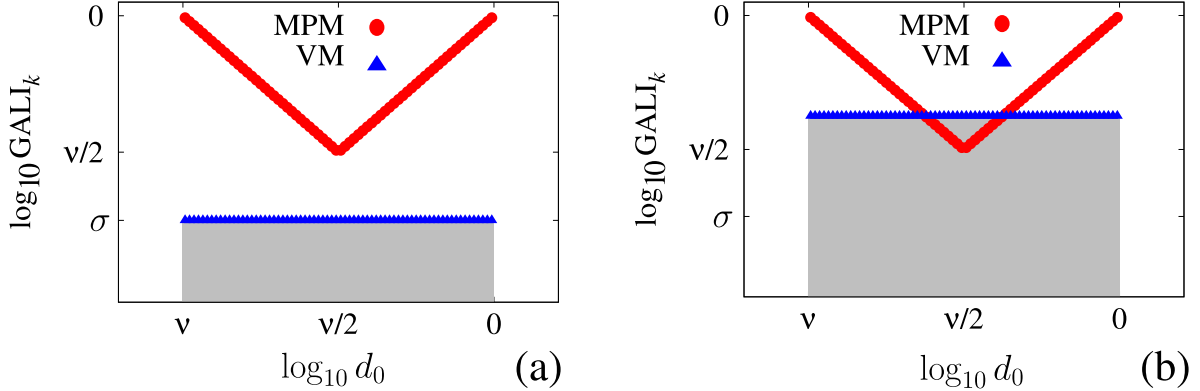


Figure 1: Theoretical reliable regions for the computation of GALI of order k with the (blue triangles) VM and (red squares) MPM with unit renormalization time, $\tau \approx 1$. The labels are as follows: $\nu = \log_{10} \varepsilon$, $d_0 = \|w_0\| = \|\delta_0\|$, $\sigma = \log_{10} \varepsilon_T$. Panel (a): $\varepsilon \lesssim \varepsilon_T \lesssim \varepsilon^{1/2}$. Panel (b): $\varepsilon^{1/2} \lesssim \varepsilon_T$.

with x_1 and x_2 , the positions, and p_1 and p_2 their associated canonical momenta. This model gives a generic description of interactions between two asymmetric celestial bodies whose motion is restricted to a two dimensional plane (e.g. the motion of a planet around its sun, a star around the center of its galaxy, etc.) or molecules with asymmetric distributions of charges. As an additional remark, the value of the Hamiltonian function itself tunes the strength of the nonlinearity.

The second model we investigate is the multidimensional β -FPUT model which consists of a chain of N coupled nonlinear oscillators. Its Hamiltonian function is expressed as [45, 37]

$$\mathcal{H}_N = \frac{1}{2} \sum_{i=1}^N p_i^2 + \sum_{i=0}^N \left[\frac{1}{2} (x_{i+1} - x_i)^2 + \frac{\beta}{4} (x_{i+1} - x_i)^4 \right], \quad (39)$$

where x_i is the displacement of the i^{th} oscillator, p_i its conjugate momentum, and the parameter β controls the strength of the nonlinear terms. The β -FPUT model is used in preference to the α -FPUT due to the absence of escaping orbits in the former, which greatly simplifies our work. The FPUT system is a generic central model in the wide and intensive field of nonlinear lattice dynamics. As such, it is involved in investigating heat conduction [46], thermalization [47, 48], ergodicity [49, 50], solitons [51], breathers [52] and chaos [53] and the possible connection between the aforementioned physical processes, see [38, 54, 55] and references therein. In our numerical simulations, we set $\beta = 1$ and tune the nonlinearity of the system by changing the value of the energy \mathcal{H}_N . Further, fixed boundary conditions (i.e., $x_0 = x_{N+1} = 0$) are assumed at the two edges of the lattice.

The models above provide a perfect setup to investigate the behavior of the chaos indicators for different dynamical regimes encountered in nonlinear systems. In that regard they are extremely appreciated in computational physics, e.g. [25, 56, 26, 29, 57]. In case of the HH, an initial condition of a specific nature can be pinpointed once we generate the Poincaré surface of section (PSS) associated with a particular \mathcal{H} [Eq. (38)] (a detailed description of the elaboration of a PSS can be found in Ref. [58]). Figure 2 depicts an example of such PSS defined by $x_1 = 0$ with $\mathcal{H} = 0.125$.

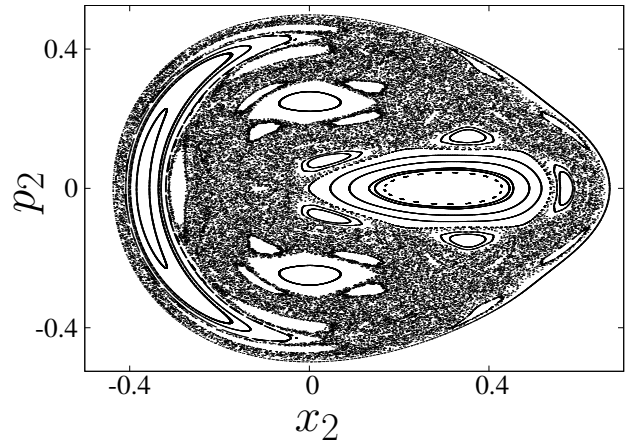


Figure 2: **2D HH system** The PSS of the HH model [Eq. (38)] at $x_1 = 0$. For each point (x_2, p_2) within the PSS, the remaining coordinates p_1 is found such that $p_1 > 0$ with $\mathcal{H} = 0.125$.

Turning now to the β -FPUT lattice model, the determination of the orbits with a specific nature is more complex mainly due to the dimensionality of the problem. Fortunately, there exist orbits which are rather simple to implement and whose vicinity has been extensively studied, the so-called *simple periodic orbits* of order 1 (SPO1) [59]. Thus in our study, we work with perturbations of these SPO1 orbits. In short, the SPO1 is a nonlinear continuation of the mode of the linearized system with wave number $\nu = (N + 1)/2$, taking the form

$$x_{2j}(0) = 0, \quad x_{2j-1}(0) = -x_{2j+1}(0), \quad (40)$$

for $j = 1, 2, \dots, \frac{N+1}{2}$ with the momentum of all particles set to $p_j(0) = 0$. Given a finite number of particles the SPO1 orbits are regular for energy values \mathcal{H}_N below the so-called first destabilization energy threshold \mathcal{H}_N^c , while being chaotic pass that threshold [59]. The \mathcal{H}_N^c can be found using the standard linear stability analysis (see [13, 60, 52, 61] for details).

During all numerical integration, we are using the symplectic ABA864 order 4 numerical scheme [62, 63, 64] which has proven to be efficient for evolving the tangent dynamics (using

the standard method for variational equations [5, 6]) for low and high precision numerical computations [27, 64]. We perform double precision computations, i.e. $\varepsilon \approx 10^{-16}$ as it is the default numeric type of almost all modern computational tasks, and required for accurate chaotic simulations. Furthermore, we control the global truncation error ε_T through the *relative energy error* E_r defined at every time $t > 0$ with

$$E_r(t) = \left| \frac{\mathcal{H}(t) - \mathcal{H}(0)}{\mathcal{H}(0)} \right|, \quad E_r^N(t) = \left| \frac{\mathcal{H}_N(t) - \mathcal{H}_N(0)}{\mathcal{H}_N(0)} \right|, \quad (41)$$

for both the HH and β -FPUT models respectively. For SIs, this means changing the integration time step h , as this quantity remains fixed during the whole evolution of the system's trajectory.

In addition the initial conditions of the set of orthogonal tangent vectors have components arising from a random uniform distribution with zero mean. Note that each component is duly rescaled to achieve the desired magnitude. For completeness sake in Appendix A we provide a general algorithm for the computation of GALI using the MPM. The program implemented using this algorithm computes the time evolution of the GALI_k up to a given time $t = T_M$. Further, it can easily be amended the perform similar tasks as for the VM counterpart (see e.g. Table 2 in Ref. [15]).

4.2. Hénon-Heiles model

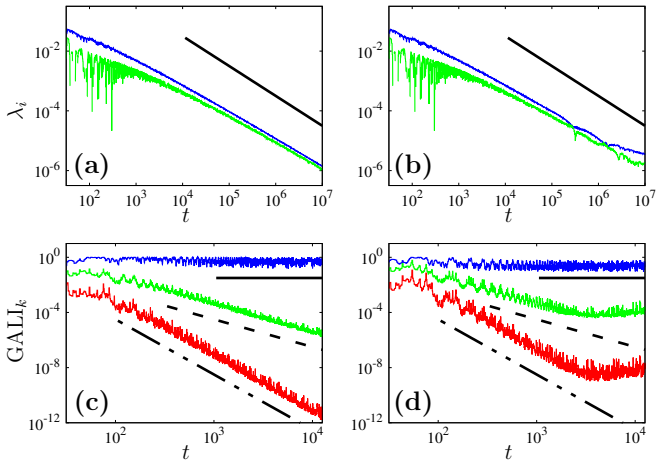


Figure 3: **2D HH system.** Time evolution of (a-b) the two largest finite-time LEs λ_1 (blue) and λ_2 (green), and (c-d) the GALI_2 (blue), GALI_3 (green) and GALI_4 (red) for a regular orbit with coordinate $x_1 = 0$, $p_1 > 0$, $x_2 = 0.558$ and $p_2 = 0$ on the Poincaré surface of section in Fig. 2 of the HH with $\mathcal{H} = 0.125$. The results are generated using the (a),(c) the VM and (b),(d) the MPM. The filled black lines in (a-b) guide the eye with slope -1 , while the filled, dashed, dotted-dotted dashed ones in (c-d) have slopes 0 [horizontal lines], -2 and -4 respectively. All the calculations are performed with $d_0 = 10^{-8}$.

We start by demonstrating that the computation of the GALI using the VM and MPM genuinely give the same results by considering initial conditions in Fig. 2. In Figs. 3 (a-b), we plot the time dependence of the two largest LEs [Eq. (4)] of the Lyapunov spectrum, λ_1 [blue curve] and λ_2 [green curve], for the initial condition of a regular orbit with $x_1 = 0$, $x_2 = 0.558$,

$p_2 = 0$ and $p_1 > 0$ evaluated such that $\mathcal{H} = 0.125$. Since we also require initial conditions for the tangent vectors, randomly selected coordinates drawn from a uniform distribution are used, and the deviation vectors are orthogonalized and rescaled to fit the desired magnitude for all tangent vectors $d_0 = 10^{-8}$. Note that we scale the deviation vector in the VM computations as good practice for comparison with the MPM.

The LEs are computed using both the VM [Fig. 3(a)] and MPM [Fig. 3(b)]. In our simulations we integrate equations associated with each method up to time $t = 10^7$ setting as integration time step $h = 0.01$ which ensures that the relative energy error is bounded by $E_r \approx 10^{-11}$. Further, we fix the renormalization time $\tau = 1$. For both methods, the computed LEs are decaying following the power law $\lambda_{1,2} \propto t^{-1}$ [black line in Fig. 3(a-b)]. This confirms that the studied orbit is regular. In addition, a divergence from the t^{-1} power law of the computed LEs through of the MPM is building up from time $t \approx 10^6$ for which the magnitude of the $\lambda_{1,2} \approx 10^{-6}$. This divergence suggests a limit in the precision of the computation of the LEs using the MPM for regular orbits [29].

Using the parameters above, we also compute the time evolution of the GALI. The numerical results of the time evolution of GALI_2 [blue curve], GALI_3 [green curve] and GALI_4 [red curve] are shown in Fig. 3(c) for the VM. In particular, we see that the VM is quite accurate in capturing the theoretical decay rates with slopes -1 , -2 and -4 in the double logarithmic scale shown using the continuous, dashed, and dotted-dotted-dashed black lines in Figs. 3(c-d). The novelty in this work, is to perform the same computations of the GALIs, using the MPM and demonstrate the effectiveness of this approach. In Fig. 3(d), we show the time evolution of the GALI_2 [blue curve], GALI_3 [green curve] and GALI_4 [red curve] computed using the MPM with the same set of tangent vectors than in the VM counterpart. This panel displays a practically constant GALI_2 which remains comparable to the one obtained using the VM, blue curve of Fig. 3(c).

On the other hand, for GALI_3 and GALI_4 an interesting trend is seen. At the early stage of the evolution, up to $t \lesssim 10^{3.5}$, the computed GALI_3 and GALI_4 are decaying following the same power laws as for the VM, black lines in Fig. 3(d). Then, for $t \gtrsim 10^{3.5}$ a levelling off to a practically constant value appears, taking the values of the computed GALI away from the expected power laws. As in case of the LEs computations, this moment marks the point from which the accumulations of numerical errors dominates the numerical values of the computed GALI.

For completeness we perform a similar analysis for a chaotic trajectory with initial coordinates on the PSS (Fig. 2) $x_1 = 0$, $x_2 = -0.25$, $p_2 = 0$ and once again $p_1 > 0$ is selected such that $\mathcal{H} = 0.125$. In Figs. 4(a-b) we plot the time evolution of the largest LEs when computed using both the VM and MPM respectively. As time evolves, the computed λ_1 for both methods show a striking resemblance, saturating to values $\lambda_1 \approx 0.045$ at large time. On the other hand, the computed second LE $\lambda_2 \propto t^{-1}$, black line in the same panels.

For this chaotic orbit, we also computed the temporal dependence of the associated GALI. In Figs. 4(c-d) we show the

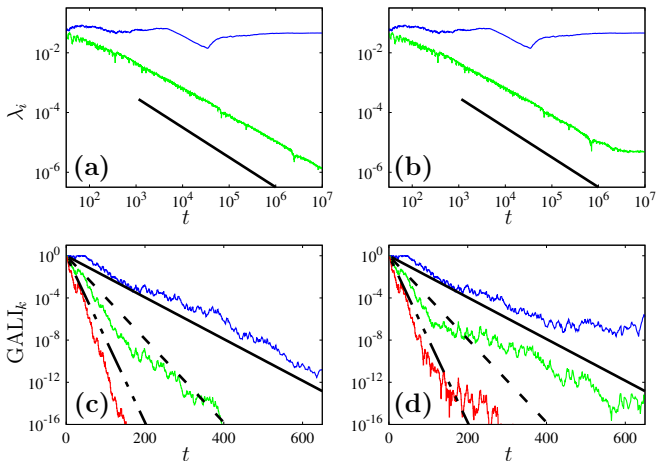


Figure 4: **2D HH system.** Same as in Fig. 3, but for a chaotic orbit with initial coordinates $x_1 = 0$, $p_1 = 0.42$, $x_2 = -0.25$ and $p_2 = 0$, on the Poincaré surface of section in Fig. 2. The filled black lines in (a-c) guide the eye with slope -1 . On the other hand the filled, dashed, dotted-dotted-dashed lines in (c-d) guide the eye with slopes $-\lambda_1/\ln(10)$, $-2\lambda_1/\ln(10)$ and $-4\lambda_1/\ln(10)$ respectively with $\lambda_1 \approx 0.0455$ at the final time of integration.

time evolution of GALI_2 [blue curve], GALI_3 [green curve] and GALI_4 [red curve]. The numerical results of the GALI_2 , GALI_3 and GALI_4 are as predicted for the VM (Fig. 4(c)), with all the values of the computed GALIs following the theoretical decay rates -0.02 , -0.04 and -0.08 respectively indicated by the continuous, dashed and dotted-dotted-dashed black lines in Figs. 4(c-d). We repeat the same simulations using the MPM and present the outcomes in Fig. 4(d). Overall, we see a good correspondence between the VM and MPM on numerical values of GALI_2 , GALI_3 and GALI_4 for time $t \lesssim 200$. Nevertheless, for $t \gtrsim 200$, a divergence from the theoretical power laws can be seen with GALI_2 practically saturating at time $t = [500, 600]$.

We now turn to estimating the practical reliable regions of the computation of the GALI by exploring its dependence on the magnitude of separation vectors d_0 . In Fig. 5, we plot GALI_2 , GALI_3 and GALI_4 at $t \approx 200$ for the chaotic orbit used in Fig. 4. In addition, we calculate results averaged over 1000 random sets of tangent vectors in order to mitigate the dependence of the computed GALI on the choice of the initial deviation vectors, (see e.g. Sec. 5.4.1.1 of Ref. [15]).

The values of GALI computed using the VM are shown in blue triangles and the values obtained through the MPM in red circles. The numerically computed GALI_2 , GALI_3 and GALI_4 using the VM are clearly independent of the magnitude of the initial deviation vectors in Figs. 5(a-c). For the MPM however, a non-trivial relation between the GALI_2 , GALI_3 and GALI_4 varying d_0 is found. Our results show V-like shapes with a global minimum value located at $d_0 \approx 10^{-8}$ for all the presented GALI. This result is in agreement with the theoretical prediction [see e.g. Fig. 1(a)] which established the global minimum at $d_0 \approx \varepsilon^{1/2}$ in a computer environment with precision ε . Consequently, in the case of double precision computation $\varepsilon \approx 10^{-16}$ the minimum occurs at $d_0 \approx 10^{-8}$.

To further probe the above observation on the numerical reliable regions above, we numerically evaluate the GALI using three different choices of the norm of the deviation vector d_0 for the regular orbit in Fig. 3. In Fig. 6, we show the time evolution of the GALI_2 , GALI_3 and GALI_4 when computed using the MPM with initial norms of the separation vectors $d_0 = 10^{-5}$, 10^{-8} and 10^{-11} [blue, green and red curves respectively], and with the VM [black curves].

In general the computation of the GALI of regular orbits is reliable in the limit of short-time for fairly small initial norms of the tangent vectors. Indeed, for all initial magnitudes of the separation vectors d_0 used in Fig. 6, the computation of GALI_2 in Fig. 6(a), GALI_3 in Fig. 6(b) and GALI_4 in Fig. 6(c) using the MPM practically overlap with the ones obtained using the VM up to $t \approx 10^3$. For larger values of the integration time $t \geq 10^3$, we expect the accumulation of numerical errors in case of the MPM to deviate the values of the computed GALIs from those obtained using the VM. Thus, based on the practical reliable regions of the MPM in Fig. 5, we expect the rate of accumulation of numerical errors to be the smallest for the case with $d_0 = 10^{-8}$. This is indeed what we observe in Fig. 6. The values of the GALI_2 , GALI_3 and GALI_4 computed with $d_0 = 10^{-8}$ [green curves in Fig. 6(a)-(c)] overlap with the results obtained with the VM for the longest integration times compared to the ones obtained using $d_0 = 10^{-5}$ and $d_0 = 10^{-11}$ [blue and red curves in Figs. 6(a)-(c)].

Let us now study the impact of the renormalization time during the computation of the GALI using the MPM. In order to reach our goal, we focus on the chaotic orbit used in Figs. 4 and 5. For our computations, we fix $d_0 = 10^{-9}$ and evolve the system's orbit and its nearby orbits up to $t \approx 200$ with $h = 0.01$. We record the final values of the GALI_2 in Fig. 7(a), GALI_3 in Fig. 7(b) and GALI_4 in Fig. 7(c) averaged over 1000 sets of initially random orthogonal separation vectors, varying τ in the interval between 0.01 to 100. We find that the dependence of the GALI on the renormalization time τ can be split into two main regions. The first region corresponds to $\tau \lesssim 1$ for which the final values of the computed GALI remain practically constant at around 5×10^{-5} , 2×10^{-10} and 1.2×10^{-18} for the GALI_2 , GALI_3 and GALI_4 respectively. On the other hand in the region where $\tau \gtrsim 1$, increasing the values of τ leads to a roughening and an overall increase in the final values of the GALI_2 , GALI_3 and GALI_4 . This results hints toward the appearance of large numerical errors in computing the GALI values.

A similar behavior is also observed when computing the dependence of the computed GALI on the integration time step h . For these numerical simulations, we kept the same set up for the numerical integration as above, setting $\tau = 1$ and varying the integration time step h . The obtained results are depicted in Figs. 7(d)-(f) for the GALI_2 , GALI_3 and GALI_4 respectively. We see that the dependence of the final value of the GALI on h can also be split into two main regions, separated by $h \approx 10^{-1}$. For $h < 0.1$, these GALI values are constant for all h , while in $h > 0.1$ we obtain different final values of the GALIs for each time step h . The striking results here is that in term of the relative energy error, $h = 0.1$ corresponds to $E_r \approx 10^{-8}$, Fig. 8. It follows that numerical simulations with relative energy error

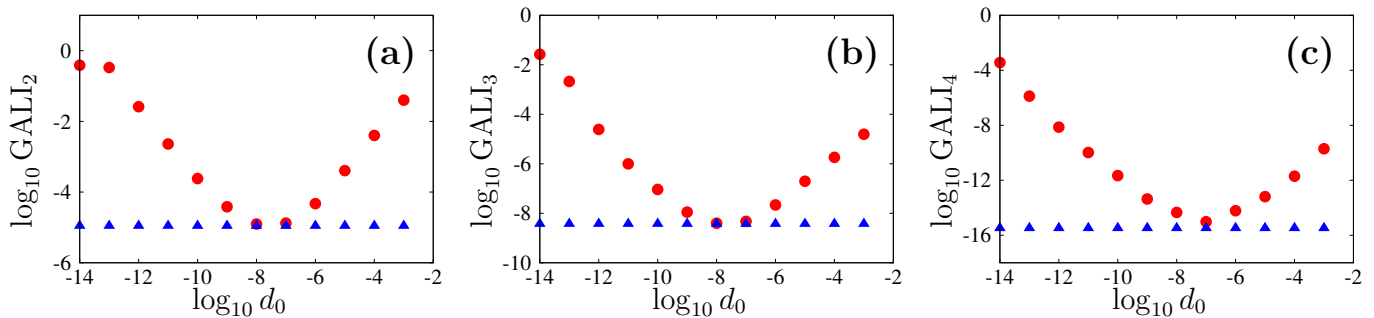


Figure 5: **2D HH system.** Dependence of GALI on the norm of the initial deviation vectors d_0 . Practical reliable regions of computation of the (a) GALI_2 , (b) GALI_3 and (c) GALI_4 of the HH using the VM (blue triangles) and MPM (red circles) methods. We averaged the GALIs over 1000 sets of orthogonal tangent vectors of norm $d_0 = \|w_0\| = \|\delta_0\|$ about the reference orbits with coordinates $x_1 = 0$, $x_2 = -0.25$, $p_1 = 0.42$ and $p_2 = 0$. The final time of integration $T \approx 200$ time units.

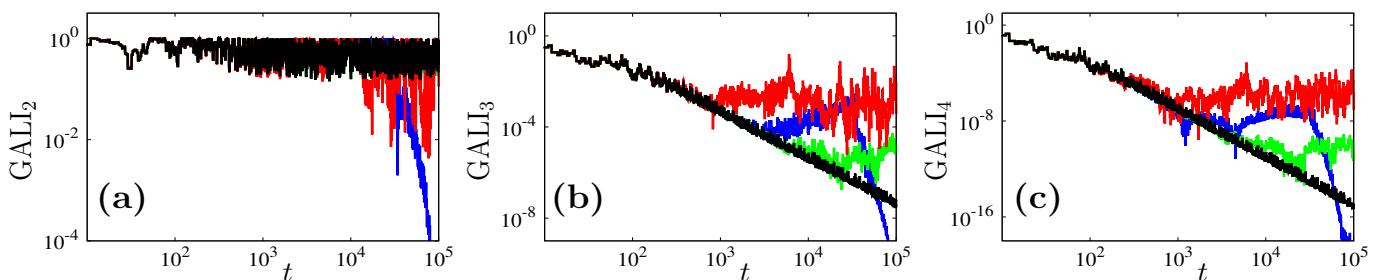


Figure 6: **2D HH system.** Time evolution of the GALI: (a) GALI_2 , (b) GALI_3 and (c) GALI_4 for an initial condition $x_1 = 0$, $x_2 = 0.558$, $p_2 = -0.1$ and p_1 is taken such that $\mathcal{H} = 0.125$, which corresponds to a regular orbit. For the MPM, we use three initial norms of the deviation vectors $d_0 = 10^{-5}$, 10^{-8} and 10^{-11} respectively the blue, green and red colored curve. The black curve in each panel represents the results obtained using the VM.

$E_r > 10^{-8}$ are in general inaccurate. Such a precision could be easily achieved using high order numerical integration schemes. It is worth pointing out the slope of the E_r against h relation which gives 4 in Fig. 8 matching the order of the integration method, see also Sec. 3.2.

What about exploring the global dynamics of a dynamical system using the GALI method with the MPM? In Fig. 9(a-b), we show the colormap of the PSS at $x_1 = 0$ of Fig. 2 made of 700×600 grid points. The remaining coordinate of each initial conditions on the (x_2, p_2) phase plane of Fig. 9 is set such that $p_1 > 0$ with $\mathcal{H} = 0.125$. Each generated orbit on the (x_2, p_2) phase plane is colored according its MLE value at $t = 1000$ [Fig. 9(a)] and GALI_2 value at $t = 500$ [Fig. 9(b)]. In addition the results are averaged over 50 configurations of sets of random orthogonal tangent vectors in order to mitigate their dependence on the choice of the initial conditions for the tangent vectors. Both chaos indicators display the same qualitative dynamical behavior in terms of characterizing the stability of orbits in the phase space.

More specifically, Figs. 9(a-b), return the same phase plane structure, that is to say the regular [yellow colored points] regions and chaotic seas [purple colored points] are practically the same in both panels and similar to what is revealed by the PSS of Fig. 2. In particular, we see that several small regular islands in the chaotic regions are well capture by the MPM, along with the so-called ‘sticky orbits’ at the interfaces of regu-

lar islands with chaotic seas with a mixed blend of colors [e.g., yellow purple]. Here the difference between the two numerical simulations resides on the computational time. Indeed, it took $t = 35.7$ and $t = 28.2$ hours respectively for the simulations of Fig. 9(a) and Fig. 9(b) to complete [65].

To the question whether we can reach the same accuracy analyzing the HH phase space with GALI of higher orders, the answer is yes. First we remind that the GALI of higher orders decrease for both regular and chaotic orbits. It follows that we need to rely on a different approach than recording the final value of the GALI as above. In order to characterize the global dynamics of the HH, we register the time it took the GALI to reach a particular threshold [15] since the GALI values tend to decay faster for chaotic orbits compared to regular ones. In Fig. 9(c), we show the time it took GALI_3 to reach the threshold 10^{-8} . This time is averaged over 50 different sets of orthogonal tangent vectors at each point once again to mitigate the dependence on the choice of the initial tangent vectors.

Clearly large decay times close to the maximal time ($t = 500$) are related to regular islands [yellow colored regions] while chaotic seas [purple colored regions] have in general smaller decay times ($t = 100 - 200$). In addition, we also find initial conditions with intermediate values of decay times, which are in general at the edge of regular islands and belong to ‘sticky’ orbits. Although we are integrating more tangent vectors than the cases above, the advantage of this method is that we can stop

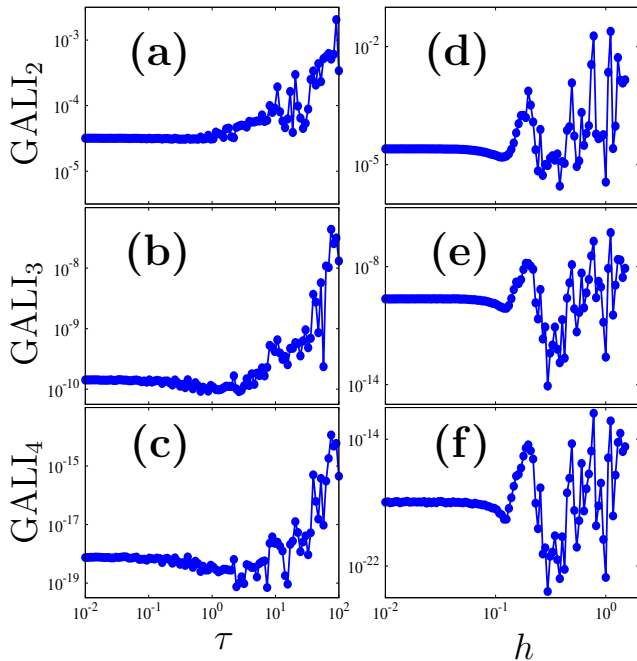


Figure 7: **2D HH system.** Dependence of GALI_2 , GALI_3 and GALI_4 on (a-c) the renormalization time τ and (d-f) the integration time step h for the chaotic orbit with $x_1 = 0$, $x_2 = -0.25$, $p_2 = 0$ and p_1 is taken such that $p_1 > 0$ with $\mathcal{H} = 0.125$. (a-c) We set the integration time step $h = 0.01$. (d-f) We fixed the renormalization time $\tau = 1$. In all computations, the final time of integration is $t = 2 \times 10^2$ with random initial deviation vectors of norm $d_0 = 10^{-9}$. The GALIs are averaged over 1000 sets of random orthogonal deviation vectors.

the simulation for each set of tangent vectors once the GALI has reached the threshold. Following this approach, we obtain a computational time $t = 28.6$ hours, close to what was obtained for the GALI_2 , despite having to integrate an extra set of tangent vectors for GALI_3 than in the GALI_2 case. Thus, the results above not only confirm the ability of the GALI method implemented using the MPM to characterize the global dynamics of Hamiltonian systems, but also demonstrates its speed compared to the MLE approach.

4.3. The β -Fermi-Pasta-Ulam-Tsingou model

We now explore the performances of the GALI method using another well-known Hamiltonian model: the β -FPUT lattice [Eq. (39)]. We first look at a small lattice, consisting of five ($N = 5$) particles, to establish the basic behaviours of the orbits we are going to study using the MLE. Knowing from the linear stability analysis that the value of the first energy destabilization threshold is $\mathcal{H}_5^c = 7.4$ for the SPO1 with $N = 5$, we choose as initial conditions (see Appendix B) perturbations of the SPO1s at fixed energy with $\mathcal{H}_5 = 5$ [Eq. (B.1)] and $\mathcal{H}_5 = 10$ [Eq. (B.2)] respectively below and above \mathcal{H}_5^c . For the integration of the equations of motion and variational equations, we fix integration time step $h = 0.02$ leading to the relative energy error being always bounded from above by $E_r^N \approx 10^{-11}$. In addition, for both method we set the renormalization time $\tau = 1$.

As a representative case, the time evolution of the MLE for the initial condition with $\mathcal{H}_5 = 5$ is presented in Fig. 10, com-

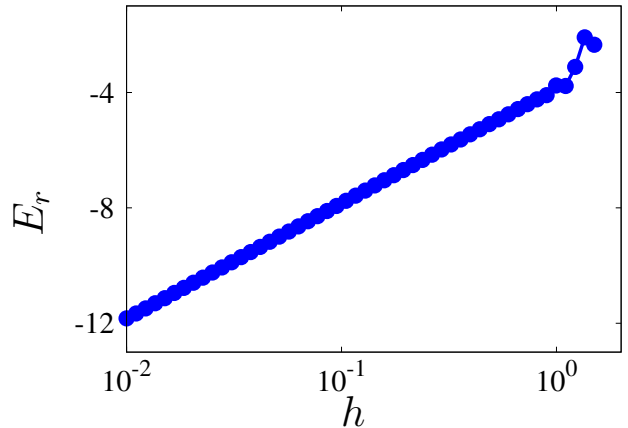


Figure 8: **2D HH system.** Dependence of the upper bound of the time evolution of the relative energy error E_r on the integration time step h . For each point in the graph the initial condition ($x_1 = 0$, $x_2 = -0.25$, $p_2 = 0$ and $p_1 > 0$ ($\mathcal{H} = 0.125$), is integrated up to $t = 200$ with the ABA864 symplectic integration scheme of order 4.

puted using the VM [continuous blue line] as well as the MPM. In the case of the MPM, we use the magnitude of the initial set of separation vectors $d_0 = 10^{-8}$ [dotted red line] and $d_0 = 10^{-11}$ [dashed green line]. As Fig. 10(a) shows, the MLE values decay towards 0 following the power law t^{-1} (shown by the black dashed line) for the VM, confirming the regular nature of the orbit we are investigating. Using exactly the same deviation vectors as for the VM for the MPM calculations, with vectors rescaled to have norms $d_0 = 10^{-8}$ and $d_0 = 10^{-11}$, both accurately track the VM result until the last stage of the evolution where the results of the separation vectors with initial norm $d_0 = 10^{-11}$ starts yielding discrepant outcomes. On the other hand for the orbit with $\mathcal{H}_5 = 10$, we can see in Fig. 10(b) that all simulations show similar time evolution of the MLE, which converge to practically constant values of the MLE at the final time of the evolution. This clearly establishes chaotic nature of the orbit above. It is worth noting that the explanations for the inaccuracy of the MPM computations of the MLE with $d_0 = 10^{-11}$ can be found in Ref. [29], in particular relating to the limitations of working too close to machine precision.

We investigate the same orbits as above using this time the GALI method. In Figs. 11(a) and (b) the black lines from the top to the bottom respectively depict the GALI_2 , GALI_4 , GALI_6 , GALI_8 and GALI_{10} calculated using the VM against time for the regular orbit with $\mathcal{H}_5 = 5$ of Fig. 10(a). In much the same way as for the HH model, the behaviour of the VM-calculated GALI values follow the theoretical predictions, irrespective of the choice of the initial size of the tangent vectors $d_0 = 10^{-8}$ [Fig. 11(a)] and $d_0 = 10^{-11}$ [Fig. 11(b)]. That is to say, we find that the time evolution of the GALI_2 and GALI_4 tend to saturate toward constant values, and the GALI_6 to GALI_{10} decay following power laws against time up to the final time of our simulations. On the other hand, the same computations performed using the MPM for GALI_2 [blue curve], GALI_4 [orange curve], GALI_6 [green curve], GALI_8

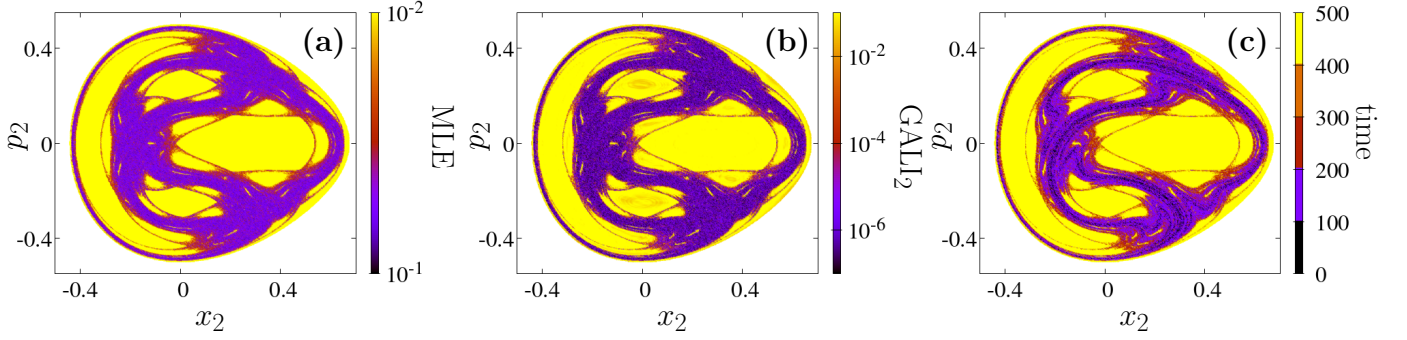


Figure 9: **2D HH system.** Regions of different dynamical behavior on the PSS of the HH at $x_1 = 0$ with $\mathcal{H} = 0.125$ [Eq. (38)] computed through (a) the MLE at $t = 1000$, (b) GALI_2 at $t = 500$. (c) Regions of different values of the time t needed for GALI_3 to become less than 10^{-8} on the same PSS section. In all computations $h = 0.01$, $\tau = 1$ and $d_0 = 10^{-8}$. In all panels, 50 sets of initial orthogonal separation vectors were used for each initial condition.

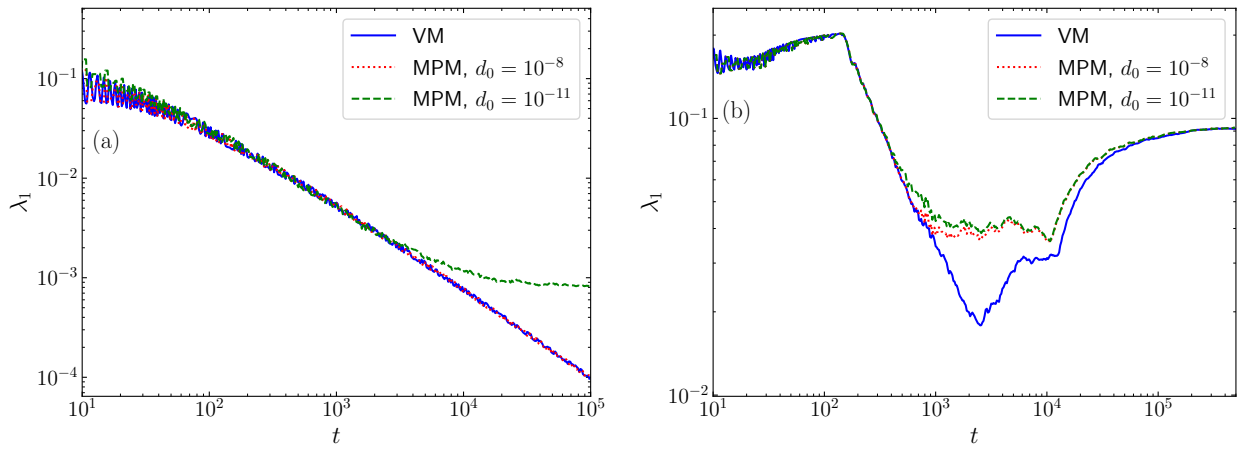


Figure 10: **β -FPUT chain.** The time evolution of the ftmLE λ_1 for two perturbations of SPO1 in the β -FPUT model with five particles: (a) A regular orbit with energy $\mathcal{H}_5 = 5$, and (b) a chaotic orbit with energy $\mathcal{H}_5 = 10$. Note that the solid lines correspond to results computed using the variational method (VM), while dotted and dashed lines show the results of the multi-particle method (MPM) with a deviation vector of norm $d_0 = 10^{-8}$ and $d_0 = 10^{-11}$ respectively. The dashed black line guides the eyes with slope ≈ -1 . In all these cases, apart from the deviation at the latest stage of the regular orbit evolution for the $d_0 = 10^{-11}$ vector, the multi-particle method accurately reproduces the variational method results.

[red curve] and GALI_{10} [purple curve] show a less trivial picture. We find that the MPM-calculated GALI values practically coincide with the ones computed using the VM, for times up to $t \approx 10^4$ for GALI_{10} and GALI_8 , while this time is much larger than our computational time in case of GALI_2 , GALI_4 and GALI_6 with $d_0 = 10^{-8}$, Fig. 11(a). However, this compatibility between the two methods lasts for a shorter time ($t \approx 10^3$) in the case of the computation using $d_0 = 10^{-11}$ in Fig. 11(b). Consequently, the deviation of the computed GALI values for growing time become more apparent in this context. Nonetheless, in both cases the computation of the GALI_2 remains rather robust since both methods return practically the same results for all simulations.

When performing the same computations using the chaotic orbits with $\mathcal{H}_5 = 10$ [Fig. 10(b)], we expect all the GALI values to decay following a power law of time. This is exactly what is demonstrated by the time evolution of the GALI_2 , GALI_4 , GALI_6 , GALI_8 and GALI_{10} [black curves from top to bottom respectively in Fig. 11(c-d)] computed using the VM with $d_0 = 10^{-8}$ [Fig. 11(c)] and $d_0 = 10^{-11}$ [Fig. 11(d)]. In

addition, the same calculation performed using the MPM tends again to follow similar temporal behaviors as that depicted by the VM for finite time $t \approx 50$. After this time, a clear deviation of the results of the MPM from those of the VM take place, now for all computed orders of the GALI.

Let us now look for the region of reliability for GALI computed with the MPM, generated using the chaotic orbit of Fig. 10(b) and Figs. 12(c-d) with $N = 5$ and $\mathcal{H}_5 = 10$. In our simulations we fix the integration time step $h = 0.02$ and evolve the dynamical equations of the system up to $t \approx 200$ time units. Further, we set the renormalization time $\tau = 1$, varying the d_0 values in the interval $[10^{-2}, 10^{-14}]$, with unit step in logarithmic scale. The GALI values at the end of the integration time are recorded, and averaged over 100 sets of random initial orthogonal tangent vectors.

In Fig. 12, the results of these computations are shown for GALI_2 , GALI_4 , GALI_6 , and GALI_8 using the VM [blue squares] and MPM [orange dots]. Clearly the numerical uncertainties of GALI_2 , GALI_4 , GALI_6 and GALI_8 do not depend on d_0 for the VM as their values remain constant for all d_0

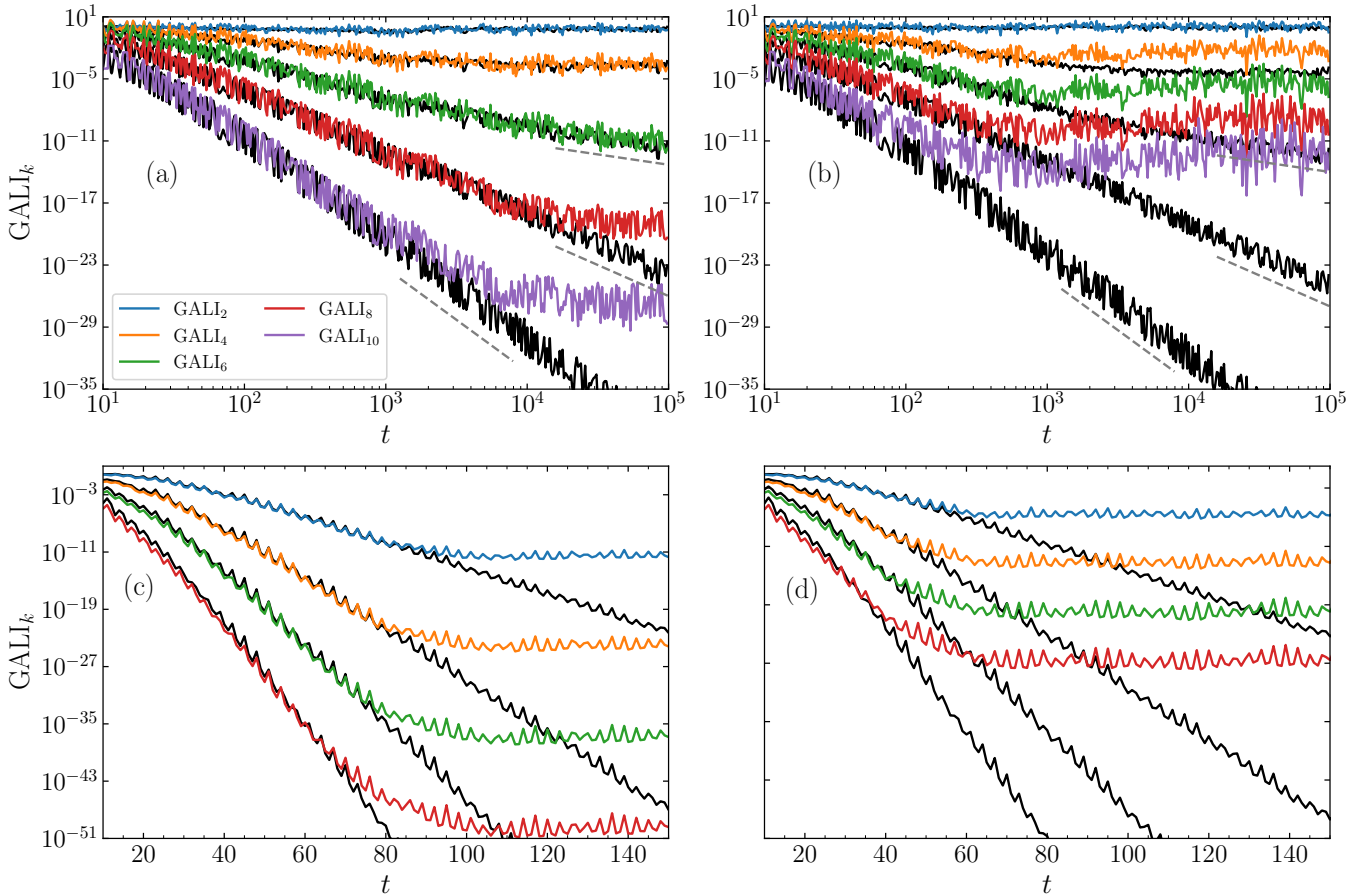


Figure 11: β -FPUT chain. Time evolution of several computed GALIs for (a) and (b): A regular orbit of the 5-particle FPUT lattice, (c) and (d): A chaotic orbit. In all cases black lines correspond to computations using the variational equations, while colored lines show the results of the multi-particle method. In (a) and (c) a deviation vector of norm 10^{-8} was used, while for (b) and (d) a norm of 10^{-11} was used. The dashed grey lines show the theoretically predicted slopes for GALI_k of regular orbits with $k > N$, according to Eq. (7). Note that in panels (a) and (b), time is plotted according to its logarithm, while panels (c) and (d) have a linear time scale.

used [blue squares in Figs. 12(a-d) respectively]. On the other hand, for the MPM simulations whose results are represented by the orange filled circles, we observe an overall V -shape of the dependence of the GALI_2 , GALI_4 , GALI_6 and GALI_8 against d_0 with the minimum located at $d_0 \approx 10^{-8}$ for all the displayed GALI. This is again in agreement with the prediction of Eq. (35).

It is worth commenting a bit more on the V -shapes in Figs. 12(a-d). This V -shape appears to be more symmetric for small GALI orders [e.g. GALI_2 in Fig. 12(a)] compared to larger ones [e.g. GALI_8 in Fig. 12(d)] with respect to the vertical line passing through the minimum and perpendicular to the horizontal axis. The same tilted V -shape was also obtained with the HH model, increasing the time at which the reliable regions are computed for GALI_3 from $t \approx 200$ [Fig. 5(b)] to $t \approx 500$ and for GALI_4 from $t \approx 200$ [Fig. 5(c)] to $t \approx 300$. Note that symmetric V -shape of the reliable region of the GALI is the consequence of the leading order term approximation of the numerical error [Fig. 1] which seems to stand firm for the GALI_2 . Consequently, the asymmetric V -shape of the reliable region of the GALI_4 , GALI_6 and GALI_8 computed at time

$t \approx 100$ in Figs. 12(b-d) respectively are indicative that the leading order approximation no longer holds for the accumulation of numerical errors. In fact, at large time lower order terms of the polynomial expansion of the numerical errors to the GALI also start contributing meaningfully to the global error.

In addition, we expect for even longer times the V -shape gives way to other asymmetrical effects, which may always possess local minimums at $d_0 \approx 10^{-8}$. However, it is remarkable to see that even past the short-time accurate region of our analysis, the estimation of the reliable region remain accurate, i.e. $d_0 \approx 10^{-8}$, which does significantly support the robustness of our findings.

It is worth emphasizing that we have found similar reliable region for the GALI method computed using the MPM with other chaotic orbits of the β -FPUT models of various lattice sizes with $N = 11$, $N = 101$, and $N = 501$ in Fig. C.13 in Appendix C. These chaotic orbits are found in the neighborhood of unstable SPO1 with energy above the first energy destabilization with $\mathcal{H}_{11}^c = 1.98$, $\mathcal{H}_{101}^c = 1.515$ and $\mathcal{H}_{501}^c = 1.502$ respectively for $N = 11$, 101 and 501.

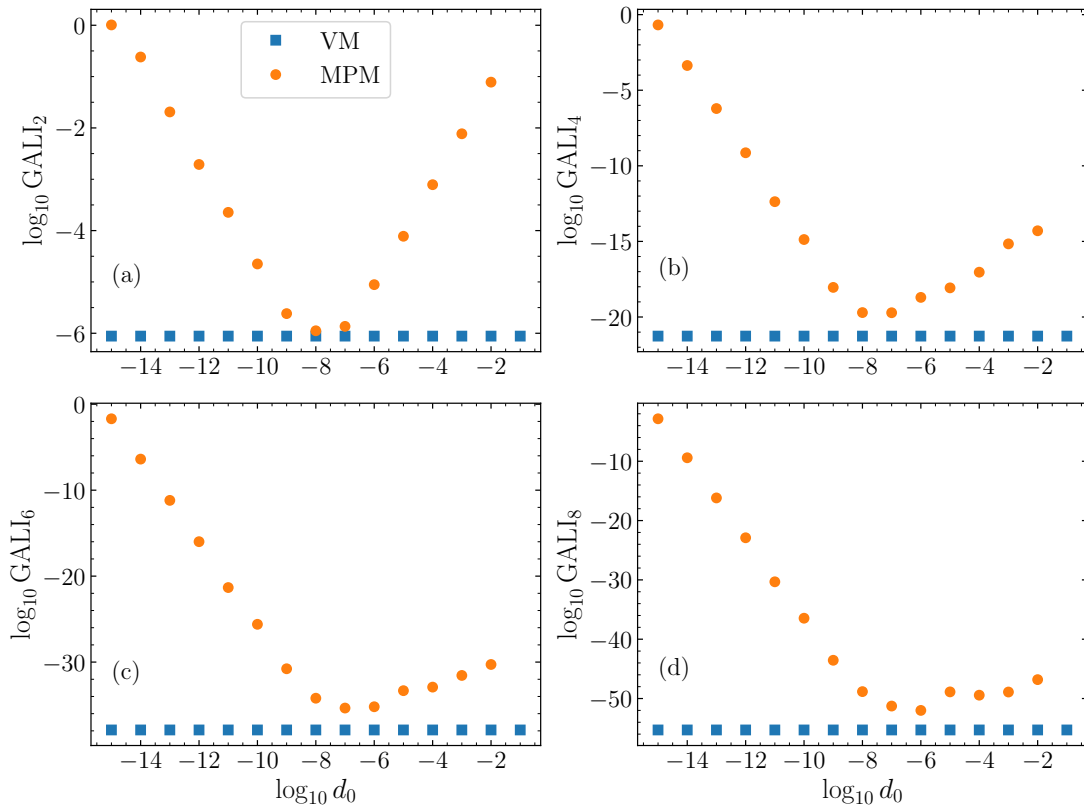


Figure 12: β -FPUT chain. Diagram of reliable regions for GALI_k in the bFPUT computed by the multi-particle method for $N = 5$, with the same chaotic initial conditions as used in Fig. 10. The total norm of the deviation vector is varied between 10^{-14} and 10^{-2} . Panels (a)-(d) correspond to GALIs of order 2, 4, 6 and 8. The blue squares are the values of GALI_k computed through the variational method, while the orange circles are the data computed via the multi-particle method. The GALI value is taken at a final time of $t = 100$.

5. Conclusion and outlook

We have shown that it is possible to accurately detect chaos in multidimensional Hamiltonian systems with the Generalised Alignment Indices (GALI), using a multi-particle method (MPM) in place of the more common but complex technique involving the variational equations, which we call the variational method (VM). We performed a theoretical and numerical analysis of the errors associated with these MPM-GALI computations, and found that for short times this method is comparable in accuracy to the VM. The errors in the calculation of GALI depend primarily on the choice of deviation vector magnitude d_0 , the renormalization time τ , and the global truncation error of the numerical integration scheme ε_T (Sec. 3). The latter being well approximated with the largest value reached by the relative energy error E_r in case of Hamiltonian systems and for numerical integration schemes with fixed integration time step. Testing these predictions on two well-known Hamiltonian models, the Hénon-Heiles (HH) and β -Fermi-Pasta-Ulam-Tsingou (β -FPUT) systems, we confirmed in Sec. 4 that for sufficiently short times, which depend on the magnitude of the GALI, the MPM results match the VM results when a reasonable deviation vector magnitude is chosen. The choice of this magnitude is discussed and tested, and based on the numerical limit of double precision accuracy $\varepsilon = 10^{-16}$, an initial deviation vector

norm of $d_0 \approx 10^{-8}$, a renormalization time $\tau \lesssim 1$ and a relative energy error $E_r \lesssim 10^{-8}$ are found to be optimal in all cases. The latter can be achieved easily using high order numerical integration schemes.

Beyond this, we also show that the MPM can be used to efficiently describe the global chaotic dynamics of the HH system, showing a clear functionality equivalent to that of the VM, and demonstrating that this technique is valid for the computation of GALIs in practice. Such high accuracy arises from the fact that short-time numerical simulations suffice to obtain a clear behavior of the GALI, in contrast with the MLE. This opens the way for GALI to be used in more complex systems, where the variational equations may be difficult/impossible to find, or simply add so much computational complexity as to be highly inefficient.

We believe this study complements existing work on the GALI method – all of which uses the VM – by enabling its application to a wider range of systems. Nevertheless, open questions remain such as considering the extension of these results to non-Hamiltonian systems, or considering short-time statistics of the GALI values for both regular and chaotic motion. This could ultimately lead to further improvements in the efficacy and speed of numerical computations with the GALI method.

Acknowledgments

The authors are grateful to Henok T. Moges for useful discussions. We thank the Centre for High Performance Computing (CHPC) of South Africa for providing the computational resources. M.H. acknowledges support from the National Research Foundation (NRF) of South Africa (Grant No. 129630).

Appendix A. Pseudo code for the computation of the GALI using the MPM

Inputs:

1. Equations of motion for the system
2. Initial conditions to integrate
3. The order k of GALI to compute
4. Initial orthogonal separation vectors, $w_i(0)$
5. Separation vector size d_0
6. Renormalization time τ
7. Time step δt
8. Final time t_f

Initialize nearby particles xn_i from deviations

for $i = 1$ to k do

$$xn_i = x + w_i$$

end

Set the next time we renormalize separation vectors to τ

$$T_{next-renorm} = \tau$$

Iterate forward from time $t = 0$ and compute GALI

while $t < t_f$ do

$$x(t) \rightarrow x(t + \delta t)$$

for $i = 1$ to k do

$$xn_i(t) \rightarrow xn_i(t + \delta t)$$

end

Check if the renormalization interval has passed

if $t > T_{next-renorm}$ do

for $i = 1$ to k do

$$xn_i = x + (xn_i - x) \times d_0 / \|xn_i - x\|$$

end

$$T_{next-renorm} = T_{next-renorm} + \tau$$

Create matrix \mathbf{A} having the unit deviation vectors as rows

for $i = 1$ to k do

$$\mathbf{A}_i = (xn_i - x) / d_0$$

end

Compute the singular values z_i of \mathbf{A}

$$z_i = \text{SVD}(\mathbf{A})$$

for $i = 1$ to k do

$$\text{GALI}_i = \prod_{j=1}^k z_j$$

end

end if

end

In the above pseudo-code, the SVD denotes the single value decomposition routine, which has demonstrated its efficiency for the computation of GALIs.

Appendix B. Initial conditions for β -FPUT lattice with $N = 5$

The initial conditions for the orbits used to compute the MLE and the GALI in Figs. 10, 11 and 12 are as follows. The regular orbit is given by

$$\begin{aligned} x_1 &= 1.03003 \\ x_2 &= 0 \\ x_3 &= -1.04003 \\ x_4 &= 0 \\ x_5 &= 1.04003 \\ p_1 &= 0.29284 \\ p_2 &= p_3 = p_4 = p_5 = 0, \end{aligned} \tag{B.1}$$

while the chaotic one reads

$$\begin{aligned} x_1 &= -1.151344372237934177 \\ x_2 &= -0.000000000000007443 \\ x_3 &= 1.151344372237925295 \\ x_4 &= 0.000000000000006056 \\ x_5 &= -1.151344372237918634 \\ p_1 &= 1.502757415151290132 \\ p_2 &= 0.000000000000014786 \\ p_3 &= -1.502757415151279696 \\ p_4 &= -0.00000000000017280 \\ p_5 &= 1.502757415151272147. \end{aligned} \tag{B.2}$$

Appendix C. Reliable regions of GALI computed using the MPM for various β - FPUT lattice sizes

In Section 4.3 we presented results for the computation of GALI using an FPUT lattice of five particles. Here for completeness we show the reliable region of the same GALIs calculated for chaotic initial conditions, of the order 2, 4, 6, and 8, computed using more degrees of freedom. Figure C.13 shows the final value of the GALIs computed with the MPM (orange circles) and the VM (blue squares) using $N = 11$, $N = 101$, and $N = 501$ particles. Here we see the same pattern as with $N = 5$, where the optimal deviation vector magnitude is around $d_0 \approx 10^{-8}$ in all cases, and an approximate if asymmetric V-shape is visible in the values of GALI computed through the MPM. As the order of the GALI increases the asymmetry of this shape increases, likely due to error terms arising from longer-time effects than predicted by the short-time theory. These results confirm that the overall findings hold true even for relatively many degrees of freedom.

References

- [1] R. C. Hilborn, Chaos and nonlinear dynamics: an introduction for scientists and engineers, Oxford University Press on Demand, 2000.
- [2] C. Skokos, G. A. Gottwald, J. Laskar, Chaos Detection and Predictability, Vol. 915 of Lecture Notes in Physics, Springer, 2016.

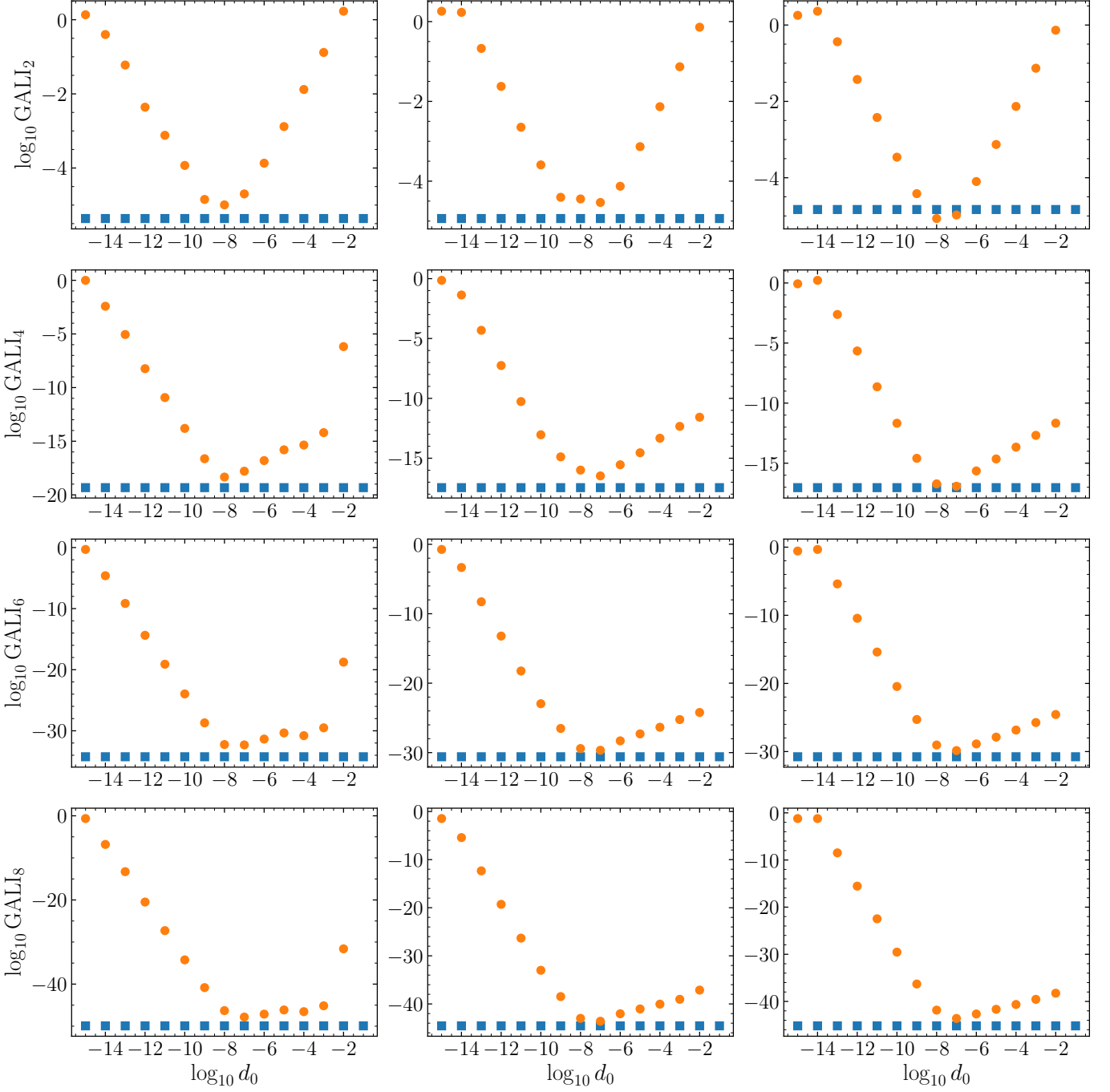


Figure C.13: **β -FPUT chain.** Diagram of reliable regions for GALL_k in the bFPUT computed by the multi-particle method for various lattice sizes. The total norm of the deviation vector is varied between 10^{-14} and 10^{-2} . Columns correspond to values of $N = 11, 101,$ and 501 respectively, while rows correspond to $\text{GALL}_2, 4, 6$ and 8 . The blue squares are the values of GALL_k computed through the variational method, while the orange circles are the data computed via the multi-particle method. The GALL value was measured at time $t = 700$ ($N = 11$), $t = 700$ ($N = 1500$), and $t = 7000$ ($N = 501$). The energies are chosen just above the critical energies $\mathcal{H}_{11}^c = 1.98$, $\mathcal{H}_{101}^c = 1.515$ and $\mathcal{H}_{501}^c = 1.502$ respectively for $N = 11, 101$ and 501 .

- [3] A. Pikovsky, A. Politi, Lyapunov exponents: a tool to explore complex dynamics, Cambridge University Press, 2016.
- [4] D. Carpintero, N. Maffione, L. Darriba, Lp-vicode: A program to compute a suite of variational chaos indicators, *Astronomy and Computing* 5 (2014) 19–27.
- [5] G. Benettin, L. Galgani, A. Giorgilli, J.-M. Strelcyn, Lyapunov characteristic exponents for smooth dynamical systems and for Hamiltonian systems; a method for computing all of them. Part 1: Theory, *Meccanica* 15 (1980) 9.
- [6] G. Benettin, L. Galgani, A. Giorgilli, J.-M. Strelcyn, Lyapunov characteristic exponents for smooth dynamical systems; a method for computing all of them. Part 2: Numerical application, *Meccanica* 15 (1980) 21.
- [7] C. Skokos, The Lyapunov characteristic exponents and their computation, *Lecture Notes in Physics* 790 (2010) 63.
- [8] E. Blumenthal, J. W. Rocks, P. Mehta, Phase transition to chaos in complex ecosystems with nonreciprocal species-resource interactions, *Physical Review Letters* 132 (12) (2024) 127401.
- [9] C. Froeschlé, E. Lega, R. Gonczi, Fast Lyapunov indicators. application to asteroidal motion, *Celestial Mechanics and Dynamical Astronomy* 67 (1997) 41.
- [10] E. Lega, M. Guzzo, C. Froeschlé, Theory and applications of the fast lyapunov indicator (FLI) method, *Lecture Notes in Physics* 915 (2016) 35.
- [11] Cincotta, P. M., Simó, C., Simple tools to study global dynamics in non-axisymmetric galactic potentials - I, *Astronomy and Astrophysics Supplement Series* 147 (2000) 205.
- [12] P. M. Cincotta, C. M. Giordano, Theory and applications of the mean exponential growth factor of nearby orbits (MEGNO) method, *Lecture Notes in Physics* 915 (2016) 93.
- [13] C. Skokos, Alignment indices: a new, simple method for determining the ordered or chaotic nature of orbits, *Journal of Physics A: Mathematical and General* 34 (2001) 10029.
- [14] C. Skokos, T. C. Bountis, C. Antonopoulos, Geometrical properties of local dynamics in Hamiltonian systems: The generalized alignment index (GALI) method, *Physica D: Nonlinear Phenomena* 231 (2007) 30.
- [15] C. Skokos, T. Manos, The smaller (SALI) and the generalized (GALI) alignment indices: Efficient methods of chaos detection, *Lecture Notes in Physics* 915 (2016) 129.
- [16] R. J. Lewis-Swan, A. Safavi-Naini, J. J. Bollinger, A. M. Rey, Unifying scrambling, thermalization and entanglement through measurement of fidelity out-of-time-order correlators in the Dicke model, *Nature Communications* 10 (2019) 1581.
- [17] J. Barré, T. Dauxois, Lyapunov exponents as a dynamical indicator of a phase transition, *Europhysics Letters* 55 (2001) 164.
- [18] M. Hillebrand, G. Kalosakas, A. Schweltnus, C. Skokos, Heterogeneity and chaos in the Peyrard-Bishop-Dauxois DNA model, *Physical Review E* 99 (2019) 022213.
- [19] M. Hillebrand, B. Many Manda, G. Kalosakas, E. Gerlach, C. Skokos, Chaotic dynamics of graphene and graphene nanoribbons, *Chaos* 30 (2020) 063150.
- [20] E. E. Zotos, F. L. Dubeibe, A. F. Steklain, T. Saeed, Orbit classification in a disk galaxy model with a pseudo-Newtonian central black hole, *Astronomy & Astrophysics* 643 (2020) A33.
- [21] E. Kovári, B. Érdi, Z. Sándor, Application of the Shannon entropy in the planar (non-restricted) four-body problem: the long-term stability of the Kepler-60 exoplanetary system, *Monthly Notices of the Royal Astronomical Society* 509 (2022) 884.
- [22] Z. Huang, G. Huang, A. Hu, Application of explicit symplectic integrators in a magnetized deformed Schwarzschild black spacetime, *The Astrophysical Journal* 925 (2022) 158.
- [23] B. Ghanbari, On detecting chaos in a prey-predator model with prey's counter-attack on juvenile predators, *Chaos Solitons & Fractals* 150 (2021) 111136.
- [24] A. F. Steklain, A. Al-Ghamdi, E. E. Zotos, Using chaos indicators to determine vaccine influence on epidemic stabilization, *Physical Review E* 103 (2021) 032212.
- [25] C. Skokos, E. Gerlach, Numerical integration of variational equations, *Physical Review E* 82 (2010) 036704.
- [26] E. Gerlach, S. Eggel, C. Skokos, Efficient integration of the variational equations of multidimensional Hamiltonian systems: Application to the Fermi–Pasta–Ulam lattice, *International Journal of Bifurcation and Chaos* 22 (2012) 1250216.
- [27] B. Senyange, C. Skokos, Computational efficiency of symplectic integration schemes: application to multidimensional disordered Klein–Gordon lattices, *The European Physical Journal Special Topics* 227 (2018) 625.
- [28] G. Tancredi, A. Sánchez, F. Roig, A comparison between methods to compute Lyapunov exponents, *The Astronomical Journal* 121 (2001) 1171.
- [29] L. Mei, L. Huang, Reliability of Lyapunov characteristic exponents computed by the two-particle method, *Computer Physics Communications* 224 (2018) 108.
- [30] M. Hillebrand, S. Zimmer, A. Ngapasare, M. Katsanikas, S. Wiggins, C. Skokos, Quantifying chaos using Lagrangian descriptors, *Chaos: An Interdisciplinary Journal of Nonlinear Science* 32 (12) (2022) 123122. doi:10.1063/5.0120889.
- [31] K. L. Johnson, Contact mechanics, Cambridge university press, 1987.
- [32] C. Lee, X. Wei, J. W. Kysar, J. Hone, Measurement of the elastic properties and intrinsic strength of monolayer graphene, *science* 321 (5887) (2008) 385.
- [33] E. Cadelano, P. L. Palla, S. Giordano, L. Colombo, Nonlinear elasticity of monolayer graphene, *Phys. Rev. Lett.* 102 (2009) 235502.
- [34] D. Wei, Y. Liu, Analytic and finite element solutions of the power-law Euler–Bernoulli beams, *Finite Elements in Analysis and Design* 52 (2012) 31.
- [35] T. Bountis, K. Kaloudis, T. Oikonomou, B. Many Manda, C. Skokos, Stability properties of 1-dimensional Hamiltonian lattices with nonanalytic potentials, *International Journal of Bifurcation and Chaos* 30 (2020) 2030047.
- [36] M. Hénon, C. Heiles, The applicability of the third integral of motion: some numerical experiments, *The Astronomical Journal* 69 (1964) 73.
- [37] J. Ford, The Fermi-Pasta-Ulam problem: Paradox turns discovery, *Physics Reports* 213 (1992) 271.
- [38] G. P. Berman, F. M. Izrailev, The Fermi-Pasta-Ulam problem: Fifty years of progress, *Chaos* 15 (2005) 015104.
- [39] M. Henon, On the numerical computation of Poincaré maps, *Physica D: Nonlinear Phenomena* 5 (2) (1982) 412–414. doi:https://doi.org/10.1016/0167-2789(82)90034-3.
- [40] S. He, K. Sun, Y. Peng, Detecting chaos in fractional-order nonlinear systems using the smaller alignment index, *Physics Letters A* 383 (19) (2019) 2267–2271.
- [41] D.-Z. Ma, Z.-C. Long, Y. Zhu, Application of indicators for chaos in chaotic circuit systems, *International Journal of Bifurcation and Chaos* 26 (11) (2016) 1650182.
- [42] W. Chatar, M. El Ghamari, J. Kharbach, M. Benkhali, R. Masrou, A. Rezzouk, M. Ouazzani-Jamil, Detecting order and chaos by the mle, sali and gali methods in three-dimensional nonlinear yang–mills system, *International Journal of Bifurcation and Chaos* 32 (10) (2022) 2250145. doi:10.1142/S0218127422501450.
- [43] C. Skokos, T. Bountis, C. Antonopoulos, Detecting chaos, determining the dimensions of tori and predicting slow diffusion in Fermi–Pasta–Ulam lattices by the generalized alignment index method, *The European Physical Journal Special Topics* 165 (2008) 5.
- [44] G. Benettin, L. Galgani, J.-M. Strelcyn, Kolmogorov entropy and numerical experiments, *Physical Review A* 14 (1976) 2338.
- [45] E. Fermi, P. Pasta, S. Ulam, M. Tsingou, Studies of the nonlinear problems, Los Alamos Report LA-1940 (1955).
- [46] T. Mai, A. Dhar, O. Narayan, Equilibration and universal heat conduction in Fermi-Pasta-Ulam chains, *Physical Review Lett.* 98 (2007) 184301.
- [47] M. Onorato, L. Vozella, D. Proment, Y. V. Lvov, Route to thermalization in the α -Fermi-Pasta-Ulam system, *Proceedings of the National Academy of Sciences* 112 (2015) 4208.
- [48] Y. V. Lvov, M. Onorato, Double scaling in the relaxation time in the β -Fermi-Pasta-Ulam-Tsingou model, *Physical Review Letters* 120 (2018) 144301.
- [49] J. De Luca, A. J. Lichtenberg, M. A. Lieberman, Time scale to ergodicity in the Fermi-Pasta-Ulam system, *Chaos* 5 (1995) 283.
- [50] C. Danieli, D. K. Campbell, S. Flach, Intermittent many-body dynamics at equilibrium, *Physical Review E* 95 (2017) 060202.
- [51] H. Zhao, Z. Wen, Y. Zhang, D. Zheng, Dynamics of solitary wave scattering in the Fermi-Pasta-Ulam model, *Physical Review Letters* 94 (2005) 025507.
- [52] S. Flach, A. V. Gorbach, Discrete breathers—Advances in theory and ap-

- plications, *Physics Reports* 467 (2008) 1.
- [53] T. Cretegny, T. Dauxois, S. Ruffo, A. Torcini, Localization and equipartition of energy in the β -FPU chain: Chaotic breathers, *Physica D* 121 (1998) 109.
- [54] D. K. Campbell, P. Rosenau, G. M. Zaslavsky, Introduction: The Fermi-Pasta-Ulam problem—The first fifty years, *Chaos* 15 (2005) 015101.
- [55] T. Dauxois, S. Ruffo, Fermi-Pasta-Ulam nonlinear lattice oscillations, *Scholarpedia* 3 (2008) 5538.
- [56] L. A. Darriba, N. P. Maffione, P. M. Cincotta, C. M. Giordano, Comparative study of variational chaos indicators and odes' numerical integrators, *International Journal of Bifurcation and Chaos* 22 (10) (2012) 1230033.
- [57] A. Choudhary, J. F. Lindner, E. G. Holliday, S. T. Miller, S. Sinha, W. L. Ditto, Physics-enhanced neural networks learn order and chaos, *Physical Review E* 101 (2020) 062207.
- [58] A. J. Lichtenberg, M. A. Leiberman, *Regular and Chaotic Dynamics*, Springer New York, NY, London, 1992.
- [59] C. Antonopoulos, T. Bountis, Stability of simple periodic orbits and chaos in a Fermi-Pasta-Ulam lattice, *Physical Review E* 73 (2006) 056206.
- [60] T. Dauxois, *Energy Localisation and Transfer*, Vol. 22, World Scientific, 2004.
- [61] H. Moges, T. Manos, C. Skokos, On the behavior of the generalized alignment index (GALI) method for regular motion in multidimensional Hamiltonian systems, *Nonlinear Phenomena in Complex Systems* 123 (2020) 153.
- [62] S. Blanes, F. Casas, A. Farres, J. Laskar, J. Makazaga, A. Murua, New families of symplectic splitting methods for numerical integration in dynamical astronomy, *Applied Numerical Mathematics* 68 (2013) 58.
- [63] A. Farrés, J. Laskar, S. Blanes, F. Casas, J. Makazaga, A. Murua, High precision symplectic integrators for the solar system, *Celestial Mechanics and Dynamical Astronomy* 116 (2013) 141.
- [64] C. Danieli, B. Many Manda, T. Mithun, C. Skokos, Computational efficiency of numerical integration methods for the tangent dynamics of many-body Hamiltonian systems in one and two spatial dimensions, *Mathematics in Engineering* 1 (2019) 447.
- [65] The codes were written in the Fortran90 language and were compiled using the gfortran compiler (<https://gcc.gnu.org/>) with the -O3 optimization flag. No advanced vectorization has been implemented.
- [66] N. Voglis, G. Contopoulos, C. Efthymiopoulos, Detection of ordered and chaotic motion using the dynamical spectra, *International Astronomical Union Colloquium* 172 (1999) 211.
- [67] C. Froeschlé, R. Gonczi, E. Lega, The fast Lyapunov indicator: a simple tool to detect weak chaos. application to the structure of the main asteroidal belt, *Planetary and Space Science* 45 (1997) 881.
- [68] C. Skokos, C. Antonopoulos, T. C. Bountis, M. N. Vrahatis, How Does the Smaller Alignment Index (SALI) Distinguish Order from Chaos?, *Progress of Theoretical Physics Supplement* 150 (2003) 439.
- [69] C. Skokos, C. Antonopoulos, T. C. Bountis, M. N. Vrahatis, Detecting order and chaos in Hamiltonian systems by the SALI method, *Journal of Physics A: Mathematical and General* 37 (2004) 6269.
- [70] M. J. Holman, N. W. Murray, Chaos in High-Order Mean Resonances in the Outer Asteroid Belt, *The Astronomical Journal* 112 (1996) 1278.
- [71] G. Contopoulos, L. Galgani, A. Giorgilli, On the number of isolating integrals in Hamiltonian systems, *Physical Review A* 18 (1978) 1183.
- [72] E. Hairer, C. Lubich, G. Wanner, *Geometric numerical integration: structure-preserving algorithms for ordinary differential equations*, Vol. 31, Springer Science & Business Media, 2006.
- [73] Z. Sándor, B. Érdi, A. Széll, B. Funk, The relative Lyapunov indicator: an efficient method of chaos detection, *Celestial Mechanics and Dynamical Astronomy* 90 (2004) 127.
- [74] J. Laskar, The chaotic motion of the solar system: A numerical estimate of the size of the chaotic zones, *Icarus* 88 (1990) 266.
- [75] G. A. Gottwald, I. Melbourne, A new test for chaos in deterministic systems, *Proceedings of the Royal Society London A* 460 (2004) 603.
- [76] C. Antonopoulos, T. Bountis, C. Skokos, Chaotic dynamics of N-degree of freedom Hamiltonian systems, *International Journal of Bifurcations and Chaos* 16 (2006) 1777.
- [77] E. Hairer, S. P. Norsett, G. Wanner, *Solving Ordinary Differential Equations I. Nonstiff Problems*, 2nd Edition, Springer, 1993.
- [78] R. Ramaswamy, Chaotic motions in vibrating molecules: The generalized Hénon-Heiles model, *Chemical Physics* 76 (1983) 15.
- [79] X. Wu, T.-Y. Huang, H. Zhang, Lyapunov indices with two nearby trajectories in a curved spacetime, *Physical Review D* 74 (2006) 083001.
- [80] G. H. Lunsford, J. Ford, On the stability of periodic orbits for nonlinear oscillator systems in regions exhibiting stochastic behavior, *Journal of Mathematical Physics* 13 (1972) 700.
- [81] B. Canbaz, Chaos classification in forced fermionic instanton solutions by the generalized alignment index (gali) and the largest lyapunov exponent, *Chaos, Solitons & Fractals* 164 (2022) 112685.
- [82] S. He, K. Sun, Y. Peng, Detecting chaos in fractional-order nonlinear systems using the smaller alignment index, *Physics Letters A* 383 (19) (2019) 2267–2271.